JGR Atmospheres

RESEARCH ARTICLE
10.1029/2024JD043037

Gravity Wave Variability in the Arctic Winter Mesosphere in Relation With the Stratospheric Polar Vortex

Subir Mandal[1], Tracy Moffat-Griffin[1], Corwin J. Wright[2], Pierre-Dominique Pautet[3], Mike J. Taylor[3], and Takuji Nakamura[4]

[1]Atmosphere, Ice, and Climate, British Antarctic Survey, Cambridge, UK, [2]Centre for Climate Adaptation and Environmental Research, University of Bath, Bath, UK, [3]Center for Atmospheric and Space Sciences, Utah State University, Logan, UT, USA, [4]National Institute of Polar Research, Tachikawa, Japan

Key Points:

- OH (3,1) band airglow images from ALOMAR were analyzed using M-transform to study gravity wave variability in the Arctic winter mesosphere
- Wind-blocking diagrams suggest that most of the observed gravity waves originated from below 50 km during January 2014, 2015, and 2016
- Gravity wave variability in Arctic winter mesosphere is strongly influenced by stratospheric polar vortex through critical-level filtering

Supporting Information:

Supporting Information may be found in the online version of this article.

Correspondence to:

T. Moffat-Griffin,
tmof@bas.ac.uk

Citation:

Mandal, S., Moffat-Griffin, T., Wright, C. J., Pautet, P.-D., Taylor, M. J., & Nakamura, T. (2025). Gravity wave variability in the Arctic winter mesosphere in relation with the stratospheric polar vortex. *Journal of Geophysical Research: Atmospheres*, *130*, e2024JD043037. https://doi.org/10.1029/2024JD043037

Received 25 NOV 2024
Accepted 9 AUG 2025

Author Contributions:

Conceptualization: Tracy Moffat-Griffin
Data curation: Pierre-Dominique Pautet, Mike J. Taylor
Formal analysis: Subir Mandal, Takuji Nakamura
Funding acquisition: Tracy Moffat-Griffin
Methodology: Tracy Moffat-Griffin
Project administration: Tracy Moffat-Griffin
Resources: Pierre-Dominique Pautet, Mike J. Taylor
Software: Subir Mandal, Tracy Moffat-Griffin, Takuji Nakamura
Supervision: Tracy Moffat-Griffin, Corwin J. Wright

Abstract In this study, we have investigated short-period (<1 hr) atmospheric gravity waves (AGWs) in the Arctic mesosphere-lower thermosphere (MLT) region during January of 2014, 2015, and 2016. We used OH (3,1) band emission data from the Advanced Mesospheric Temperature Mapper (AMTM) at the Arctic Lidar Observatory for Middle Atmosphere Research (ALOMAR), Norway. By applying a three-dimensional spectral analysis technique (Matsuda-transform), we derived phase velocity spectra of AGWs and characterized both intraday and day-to-day variability by examining wave power across multiple directional bins and phase speed ranges. Our results reveal significant year-to-year differences in AGW activity with markedly reduced spectral power and shifted propagation directions in January 2015 compared to 2014 and 2016. We compared these wave characteristics with the directional distribution of critical-level filtering between 0 and 50 km, utilizing ERA5 reanalysis winds and with the Arctic Oscillation (AO) index. We found that dominant wave propagation directions closely aligned with critical-level filtering below 50 km and that the reduced AGW activity in January 2015 was associated with stronger polar vortex conditions (higher AO values). In contrast, weaker polar vortex conditions (lower AO values) in 2014 and 2016 allowed more diverse AGW spectra to reach mesospheric altitudes. These findings highlight the crucial role of stratospheric wind structures in driving AGW variability in the Arctic MLT region during winter.

Plain Language Summary In this work, we have studied gravity waves, which are oscillations in the atmosphere driven by buoyancy forces in the polar regions of Earth's upper atmosphere. These waves are typically generated in the lower atmosphere and travel upward, where they eventually break and deposit their energy. This process can change wind patterns, and temperatures in the upper atmosphere. By monitoring fluctuations in the brightness of atmospheric emissions originating near 87 km altitude, we determined how fast the waves were moving and in which directions. Our results show notable differences in wave activity during January 2015 compared to the same period in 2014 and 2016. Further analysis revealed that these differences were mainly caused by wind patterns in the upper stratosphere, which can block gravity waves from reaching higher altitudes. Understanding how these winds influence gravity waves is important for improving atmospheric models, thereby enabling better prediction of conditions in the upper atmosphere, especially in polar regions.

1. Introduction

The majority of atmospheric gravity waves (AGWs) present in the mesosphere–lower–thermosphere (MLT) region (80–120 km) are generated by lower atmospheric sources such as orography (M. J. Alexander & Teitelbaum, 2007; Fritts et al., 2016; Hindley et al., 2021; Moffat-Griffin et al., 2013; Pautet et al., 2019), convective activity (M. J. Alexander & Pfister, 1995; M. J. Alexander et al., 2000; Sato et al., 1995; Singh & Pallamraju, 2016), wind shears (Fritts, 1982, 1984; Pramitha et al., 2015; Scinocca & Ford, 2000), and the stratospheric polar vortex (S. Alexander et al., 2011; O'Sullivan & Dunkerton, 1995; Yoshiki & Sato, 2000; Yoshiki et al., 2004). As these AGWs propagate away from their sources, their ability to reach the upper atmosphere depends on various dissipation mechanisms, including radiative damping, nonlinear wave–wave interactions, eddy diffusion, molecular diffusion, kinematic viscosity, thermal conduction, and ion-drag (Pitteway & Hines, 1974; Vadas, 2007; Vadas & Fritts, 2005; Yiğit et al., 2009). Atmospheric gravity wave dissipation results in the deposition of energy and momentum into the background flow, altering wind and temperature structures and driving large-scale circulation, including the cold summer and warm winter mesopause structure observed at

Validation: Subir Mandal
Writing – original draft: Subir Mandal
Writing – review & editing: Tracy Moffat-Griffin, Corwin J. Wright

high-latitudes (Becker, 2012; Fritts & Alexander, 2003; Lindzen, 1981; Vincent, 1984). Short-period (<1 hr) AGWs with smaller horizontal scales are particularly effective at vertically transporting momentum (Fritts & Vanzandt, 1993; Lindzen, 1981; Reid & Vincent, 1987).

Additionally, AGWs can be absorbed into the background mean flow through a process known as "critical-level filtering," which occurs when their horizontal phase speed matches the ambient wind speed (Booker & Bretherton, 1967; Hines & Reddy, 1967). Importantly, AGWs that propagate against the background wind direction are Doppler-shifted to longer vertical wavelengths, making them easier to detect using airglow imaging. In contrast, waves that propagate with the background wind are Doppler-shifted to shorter vertical wavelengths, increasing the likelihood of cancellation and reduced visibility (Z. Li et al., 2011; J. Li et al., 2020; Liu & Swenson, 2003). In high-latitude regions during winter, the stratospheric polar vortex forms as a strong circumpolar westerly jet, characterized by strong eastward winds encircling the polar region, typically centered around 50–70° latitude region (Andrews et al., 1987; Matsuno, 1971). Upward propagating AGWs can be reflected downward by the edge of the stratospheric polar vortex (Moffat-Griffin et al., 2013; Sato et al., 2012). Seasonal and year-to-year changes in the strength and vertical extent of the vortex can act as a major driver of variability in upward-propagating AGWs. Previous studies have reported observations of westward propagating AGWs in the MLT during winter are related to critical-level filtering of eastward waves in the upper stratosphere (Q. Li et al., 2016; Nakamura et al., 1999). Therefore, studying the horizontal phase velocity spectra of short-period AGWs is crucial to understanding their propagation and variability in the MLT region (Fritts & Alexander, 2003; Taylor et al., 1993).

In recent decades, variability in the MLT region has been studied using various measurement techniques, such as sounding rockets, radars, airglow observations, lidars, and satellites (Goldberg et al., 2006; Mertens et al., 2001; Mitchell et al., 2002; Pallamraju et al., 2014; Singh & Pallamraju, 2017; Taylor, Bishop, & Taylor, 1995; Taylor, Turnbull, & Lowe, 1995; Vincent, 1984). Among these, ground-based airglow imaging is particularly valuable for investigating the horizontal structure and phase speeds of short-period and small-scale AGWs. As these waves propagate through the airglow layers, they induce density and temperature perturbations that affect local chemistry, which manifest as variations in emission intensity detectable from the ground. A variety of optical instruments, such as photometers, interferometers, spectrometers, and imagers, have been used to monitor airglow fluctuations to study AGWs (Gardner, 1991; Taylor, Bishop, & Taylor, 1995; Taylor, Turnbull, & Lowe, 1995). Since their discovery by Meinel (1950), airglow emissions originating from the rotation–vibration bands of hydroxyl (OH) radicals have been extensively used to study MLT dynamics, as they are the brightest compared to other emissions (O_2, Na, & OI) from this part of the atmosphere (Wallace, 1962). The OH band emission layer is centered at 86.8 ± 2.6 km and has a thickness of 8.6 ± 3.1 km with the exact height of the emission peak depending on the vibrational levels (Baker & Stair, 1988; von Savigny et al., 2012; Wüst et al., 2023). Conventionally, OH (6,2) and (8,3) band emissions in the 700–800 nm wavelengths are used to study the MLT region, as they can be easily detected by CCD-based cameras (Krassovsky & Shagaev, 1977; Myrabø et al., 1987; Singh & Pallamraju, 2017; Takahashi et al., 1985; Taylor & Hill, 1991). However, in the high-latitudes, these spectral regions are often strongly contaminated by aurora emissions making them less suitable for AGW studies. The OH emissions from the (3,1) and (4,2) bands around 1,520 and 1,600 nm, respectively, provide significant advantages for observing the MLT region at high-latitudes, as they are not only brighter and less affected by water vapor absorption compared to the (6,2) and (8,3) bands but also allow for longer-duration observations under aurora and full moon conditions (Pautet et al., 2014, 2019; Singh et al., 2023).

Methodologies for analyzing airglow images to obtain information on AGWs have significantly advanced over the years. Traditionally, these analyses involved manual identification of wave features in images (Hapgood & Taylor, 1982; Lanchester, 1985; Taylor et al., 1997; Taylor & Hapgood, 1988) and applying Fourier analysis to images projected onto a uniform grid of geographical distances (Coble et al., 1998; Garcia et al., 1997; Hecht et al., 1994; Hindley et al., 2016; Wright et al., 2017). However, these conventional approaches often provide limited insight into the full horizontal phase velocity distribution, which is essential for assessing filtering effects on upward-propagating waves. Matsuda et al. (2014) proposed an innovative approach to derive power spectra of airglow intensity variations in the horizontal phase velocity domain (referred to as phase velocity spectra) from a sequence of airglow images expanding upon the three-dimensional (3D) analysis method described by Coble et al. (1998). This technique has enabled long-term analysis and comparison of AGWs and traveling ionospheric disturbances across multiple airglow observation locations without the human bias involved in identifying wave-like features in images (Perwitasari et al., 2018; Takeo et al., 2017; Tsuchiya et al., 2018, 2019).

Ground-based observations of AGWs in polar regions using airglow imaging are considerably fewer than those in low and mid-latitudes primarily due to challenging environmental conditions and contamination of images by aurora. Although several recent studies have examined AGW activity at high-latitudes, the majority were conducted in the Antarctic region (Espy et al., 2004; Kam et al., 2021; Kogure et al., 2021; Matsuda et al., 2017; Nielsen et al., 2012) with only a few in the Arctic (J. Li et al., 2020; Suzuki et al., 2009; Wüst et al., 2019). The OH (3,1) band emission intensity images obtained from the Advanced Mesospheric Temperature Mapper (AMTM) at the Arctic Lidar Observatory for Middle Atmosphere Research (ALOMAR; 69.38°N, 16°E) in Norway thus provide a unique opportunity to enhance our understanding of AGW variability in the Arctic MLT region. In this study, we derived AGW phase velocity spectra for wave periods of 5–60 min and horizontal wavelengths of 10–100 km by applying the M-transform (Matsuda et al., 2014) to preprocessed OH (3,1) intensity maps collected during January 2014, 2015, and 2016. These months were selected based on the availability of continuous sequences of images that were largely free from cloud and auroral contamination, allowing investigation of short-period AGW variability under differing stratospheric polar vortex conditions. Spectral power were computed across different phase speed ranges and propagation directions to examine intraday, day-to-day, and year-to-year variability. These results are further interpreted in the context of critical-level filtering using wind-blocking diagrams constructed from ERA5 reanalysis winds.

2. Instrument and Data Sets

2.1. Advanced Mesospheric Temperature Mapper (AMTM)

Multiple AMTMs have been developed by Utah State University, USA and are operated at various locations to obtain two-dimensional (2D) intensity and temperature maps of the OH (3,1) band emissions. The AMTM measures $P_1(2)$, $P_1(4)$ line emissions and a background region (BG) over 120° field of view (FOV) using three narrow band filters centered at 1,523, 1,542, and 1,521 nm, respectively, with exposure times of 10 s each. These emissions are imaged on a 320 × 256 pixel array of the Indium-gallium-arsenide (InGaAs) detector and are corrected for non-uniform response of the InGaAs detector, filters, and optics. Subsequently, the rotational temperature and relative OH (3,1) band intensity are calculated for each pixel resulting in two new images: a rotational temperature map and a band intensity map (Pautet et al., 2014). These images are then spatially calibrated using the known background stars and projected onto a 180 × 144 km linear grid to correct for the lens format, assuming 87 km as the altitude of peak OH emission (Garcia et al., 1997; Pautet & Moreels, 2002). The AMTM provides intensity and temperature maps from OH (3,1) band emissions approximately every 30 s, which is much shorter than the Brunt-Väisälä period in this region.

Figure 1a illustrates the geographical location of the ALOMAR AMTM. An example of OH (3,1) band emission intensity map recorded at 03:15 UT on 11 January 2014 by the AMTM at ALOMAR is presented in Figure 1b. The distorted shapes visible at the bottom and top-right corner of the intensity map are due to the projection onto a uniform geographical grid. To mitigate these distortions, the intensity maps were cropped from 320 × 256 pixels to an area of 230 × 230 pixels centered around the zenith of the field of view as depicted in Figure 1c. The spatial extents of the FOV around the ALOMAR station for the images shown in Figures 1b and 1c are marked by red and blue rectangles, respectively, in Figure 1a. The accuracy of the AMTM data has been validated by comparing the temperature derived using the line-pair ratio method with those from co-located lidar observations. Further details of the instrument design, operation, and data validation for the AMTM can be found in Pautet et al. (2014). These two-dimensional OH intensity and temperature maps have been used to study gravity wave momentum flux and retrieval of intrinsic wave parameters in the Scandinavian region (Fritts et al., 2014; Reichert et al., 2019), large-scale oscillations in mesospheric temperatures, frontal gravity wave activity, and horizontal phase velocity distribution of AGWs in Antarctica (Kogure et al., 2023; Pautet et al., 2018; Zhao et al., 2019), mountain waves and their breaking in the MLT region (Fritts et al., 2016; Pautet et al., 2021; Taylor et al., 2019), and the effects of wind shear on the propagation of AGWs and Kelvin-Helmholtz instability structures in midlatitudes (Fritts et al., 2023; Yuan et al., 2024).

The 2D intensity and temperature maps, along with the data quality catalog for the ALOMAR AMTM, were provided by coauthors from Utah State University. The AMTM observations made from ALOMAR during January 2014, 2015, and 2016 had the longest continuous sequences of good quality (defined in Section 3.1) OH images. Notably, there were no sudden stratospheric warming events (SSWs) during these periods, which are known to strongly influence middle atmospheric dynamics. In line with previous studies that analyzed AGW

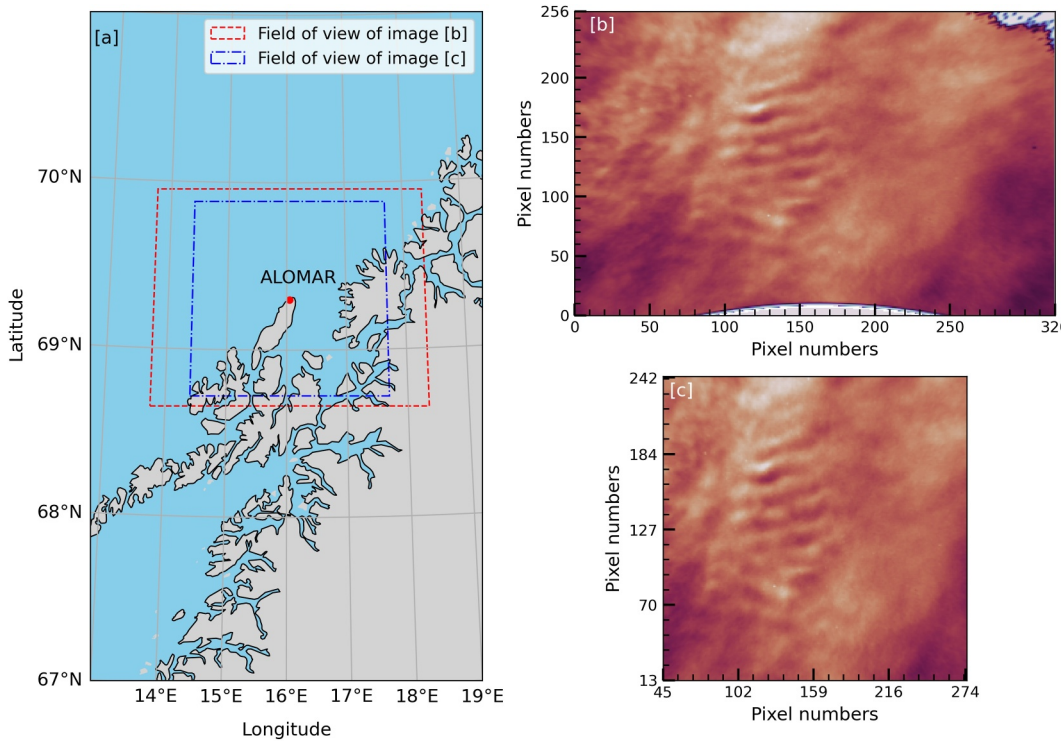

Figure 1. (a) The geographical location of the ALOMAR AMTM. Landmasses are shown in light-gray, while ocean and water bodies are in sky-blue with black coastlines. (b) A typical OH intensity map (320 × 256 pixels) projected onto a uniform geographical grid obtained from raw images at 03:15 UT on 11 January 2014. Distortions at the bottom and right corner of the image are artefacts resulting from the projection process with a geographical distance of 562.5 m between two successive pixels in both *X* and *Y*-directions. (c) This is the same OH intensity map now cropped to a 230 × 230 pixel region centered around the zenith to exclude areas distorted by projection. The fields of view for the intensity maps in panels (b) and (c) are delineated by red and blue rectangles, respectively, in panel (a).

phase velocity spectra using AMTM intensity maps from Antarctica (Kogure et al., 2023; Matsuda et al., 2017), we only used OH (3,1) band intensity maps from ALOMAR AMTM (as shown in Figure 1). The data from these specific months were selected to investigate the winter-time variability of AGWs in the Arctic MLT region.

2.2. ERA5 Winds

The ERA5 data set, the latest global climate reanalysis produced by the European Centre for Medium-Range Weather Forecasts (ECMWF), is based on a numerical weather prediction model and data assimilation system. It incorporates a vast array of observational data from various sources, including satellites, radiosondes, and ground-based instruments to provide a comprehensive and consistent representation of the global atmosphere. ERA5 provides hourly data on multiple vertical coordinate systems, including standard pressure levels and its native 137 model levels, allowing for the analysis of atmospheric variables from the surface up to 80 km. The data cover the Earth on a 31-km grid (Hersbach et al., 2020). In this study, we used only hourly background wind data from ERA5, restricting to the altitude range of 0–50 km within a ±5° latitude and longitude region centered over ALOMAR due to the reduced reliability of ERA5 winds at higher altitudes. These winds were utilized to generate wind-blocking diagrams based on the principles of critical-level filtering.

2.3. Arctic Oscillation (AO) Index

The Arctic Oscillation (AO) index quantifies the state of atmospheric circulation over the Northern Hemisphere and is a dimensionless value. It is derived from the leading empirical orthogonal function (EOF) of monthly mean sea-level pressure anomalies poleward of 20°N and is characterized by anticlockwise winds around the Arctic typically near 55°N latitude (Thompson & Wallace, 1998). A positive AO index corresponds to a strengthened and contracted polar vortex with lower than average geopotential heights over the Arctic and higher than average

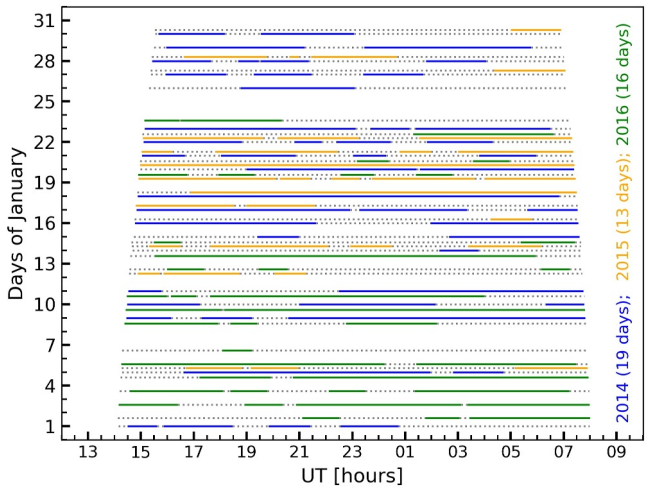

Figure 2. Time ranges of continuous good quality (not contaminated by clouds, the moonlight, & the aurora) OH images obtained from the ALOMAR AMTM are shown as solid lines for January of 2014 (blue), 2015 (yellow), & 2016 (green). Dotted lines connecting the solid-colored lines represent the duration of AMTM operation on a given day. Times on the *X*-axis are shown in UT.

heights at mid-latitudes. In contrast, a negative AO index indicates a weakened and expanded polar vortex characterized by higher than average geopotential heights in the polar region and lower heights at mid-latitudes. For this study, we used the daily values of the AO index at the 1,000 hPa pressure level as indicators of the stratospheric polar vortex strength in the Northern Hemisphere.

3. Data Selection and Analysis Techniques

3.1. Selection of OH-Airglow Images

As with any other ground-based airglow data set, the OH images obtained by the ALOMAR AMTM are susceptible to contamination from clouds, the moonlight, and aurora within the instrument's field of view. To mitigate this, we manually inspected each image from these months before proceeding with further analysis. This step is crucial to prevent artificial wave-like features from appearing in the spectral analysis, which could be introduced by these contamination sources. The availability of continuous contamination-free OH images during January in these 3 years allow us to conduct spectral analyses to investigate the winter-time variability of AGWs in the MLT altitudes. Figure 2 illustrates the observation duration and availability of "good images," which are free from intensity variations caused by clouds, the moonlight, and aurora. The duration of good images in January 2014, 2015, and 2016 are represented by blue, orange, and green solid lines, respectively. These lines indicate the time ranges when contamination-free images were continuously available for at least 60 min (i.e., consecutive 90 images or more). This criterion was chosen because our focus is on AGWs with smaller horizontal wavelengths and periods shorter than 1 hr, as these waves have been shown to contribute approximately 70% of the AGW momentum budget (Fritts & Vanzandt, 1993; Reid & Vincent, 1987).

The ALOMAR AMTM operates during the winter months and is programmed to capture images daily when the solar zenith angle exceeds 98°. In Figure 2, the endpoints of the dotted lines connecting the solid-colored lines represent the total duration of observation for each day. The trapezoidal shape of the observation duration results from the decreasing length of nighttime periods in the Arctic as January progresses, which reduces the operational time for the ALOMAR AMTM. Consequently, based on the criteria for selecting continuous data for our analyses discussed previously, OH intensity maps were available for 19, 13, and 16 days in January of 2014, 2015, and 2016, respectively. These maps were then used as input for the M-transform routine (Matsuda et al., 2014) to obtain phase velocity spectra of the AGWs observed around the emission altitude region of the OH (3,1) band.

3.2. The Matsuda-Transform

The traditional approach of estimating the spatial characteristics of AGWs from a series of airglow images involves identifying wave features in the images and tracking their movement across the field of view in multiple images along with performing spectral analyses. These event-based analyses are time consuming and prone to human bias, as they often rely on identifying waves only when their amplitude of perturbations is strong. Matsuda et al. (2014) introduced a novel spectral analysis method, M-transform, for the characterization of AGWs using airglow imaging data. This method provides the phase velocity spectra of AGWs from a series of airglow images for a given range of horizontal wavelengths and time periods. Such phase velocity spectra of AGWs offer direct visualization of the distribution of wave energy as functions of propagation speeds and directions.

Before inputting airglow images into the M-transform, they need to be preprocessed following specific procedures. This preprocessing involves projecting the raw images onto a geographical coordinate system with equal distances along latitudinal and longitudinal directions (Garcia et al., 1997; Narayanan et al., 2009) and then generating normalized perturbation images at each time by subtracting the temporally averaged background from each image. The M-transform routine then applies a 2D prewhitening filter and a 2D Hanning window to each of these preprocessed images to reduce the contamination of higher wavenumbers with lower wavenumber peaks in the AGW spectrum and to mitigate the effects of discontinuity due to the finite spatial window of the images (Coble et al., 1998). The M-transform subsequently computes the 3D power spectral density (PSD) as a function

of wavenumbers and frequency from this time sequence of processed images using a fast Fourier transform (FFT). These wavenumber spectra are then converted to phase-velocity spectra (PSD as functions of zonal and meridional phase speeds and frequencies) using coordinate transformation. Finally, these are integrated over the entire frequency range to generate two-dimensional phase velocity spectra of AGWs. The phase velocity spectra of AGWs obtained by applying M-transform to the images have shown excellent agreement with those from conventional event-based analysis on a data set collected at Syowa Station, Antarctica (Matsuda et al., 2014). This technique enables efficient and unbiased analysis of large airglow data sets for AGWs and captures a wider spectrum of AGWs, including the faint waves that might be missed in manual identification of them on the image. Further details on the application of the M-transform procedure to airglow images for characterizing AGWs, and to GPS-derived total electron content for studying traveling ionospheric disturbances, are available by Matsuda et al. (2014) and Perwitasari et al. (2022), respectively.

For the OH intensity maps obtained from the ALOMAR AMTM, additional preprocessing was necessary before applying the M-transform. First, hot pixels and stars were identified using an absolute intensity threshold and removed by replacing the corresponding pixel values using a median filter with a window size of 15 × 15 pixels. Next, the images were cropped to 230 × 230 pixels, centered around the zenith of the field of view, covering approximately 129 km × 129 km of geographical area. In the OH intensity maps shown in Figure 1c, the uniform spacing between successive pixels in both the X and Y directions is 562.5 m.

Normalized perturbation images for each OH intensity map were created using Equation 1 (Matsuda et al., 2014):

$$\frac{I'}{\bar{I}} = \frac{I - \bar{I}}{\bar{I}} \tag{1}$$

Here, I' represents the value at a specific pixel of the perturbation image, I denotes the counts at that pixel in the OH intensity map, and $\bar{I}$ is the temporally averaged value at that pixel over the time window used as input to the M-transform. Following the methodology of Matsuda et al. (2014), we derived the phase velocity spectra by applying the M-transform to these perturbation images using predefined wave parameter ranges : horizontal wavelengths of $10 - 100$ km, ground-based wave periods of $5 - 60$ min, and observed phase speeds of $0 - 150$ m/s. The M-transform analysis was conducted only when at least 90 consecutive images were available ensuring at least one hour of continuous data. This analysis was carried out for all good images on each day as shown in Figure 2.

The phase velocity spectra of AGWs derived from the OH intensity maps for each day were combined to represent the daily behavior of gravity waves. An example of such daily averaged output for all images on 05–06 January 2016 is shown in Figure 3. The concentric circles in the figure indicate phase speeds of AGWs, incrementing by 10 m/s from 0 to 150 m/s, with the color map showing the spectral power of gravity waves as a function of their propagation speeds and directions. The topmost and rightmost points of the spectra represent the geographic north and east directions, respectively. These AGW phase velocity spectra from the intensity maps (shown in Figure 3) offer better contrast compared to those derived from the corresponding temperature maps of the ALOMAR AMTM. A representative comparison between the two is provided in the supplementary material (Figure S1). The apparent motion of the Milky Way galaxy in the image FOV during observations can contaminate the phase velocity spectra between 0 and 20 m/s (Matsuda et al., 2014). Therefore, we masked the 0–20 m/s range (blue shaded region), of the spectra, as illustrated in Figure 3, for better visualization. The PSD values in this region were excluded from further analysis in the quantification of AGW activity. This also implies that orographic gravity waves are being indirectly filtered out from our analyses. The strong spectral power in the first quadrant of the spectra in Figure 3 suggests that the gravity waves predominantly had phase speeds between 20 and 50 m/s and were propagating northeastward. Similar outputs from other days with good images were further analyzed to study the day-to-day variability of AGW activity in the MLT region.

3.3. Wind-Blocking Diagrams

As discussed in Section 1, critical-level filtering of upward-propagating AGWs by background winds is a key driver of day-to-day variability in the AGW spectra observed at MLT altitudes. At the critical level, where the wave phase speed matches the background wind speed, the intrinsic frequency of the wave approaches the inertial frequency, leading to an infinite vertical wavenumber. As a result, the wave is dissipated and absorbed into the

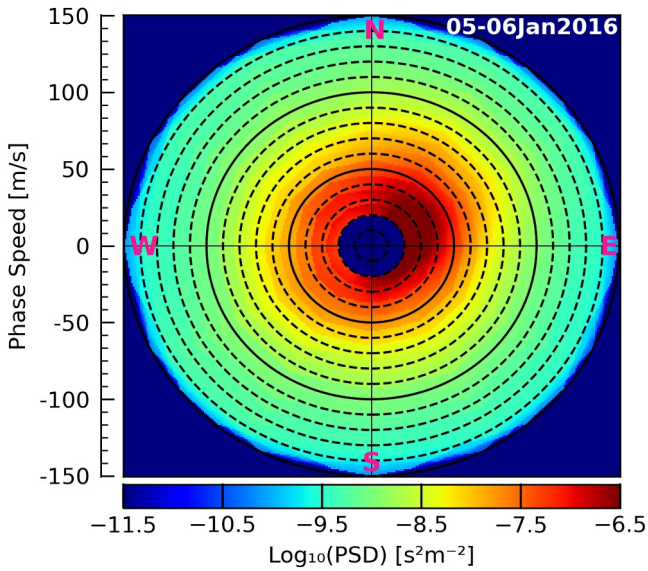

Figure 3. Phase velocity spectra of atmospheric gravity waves (AGWs) for 05–06 January 2016 obtained by applying the M-transform to the time series of OH (3,1) band emission intensity maps is shown here. The concentric circles represent phase velocities ranging from 10 m/s (innermost) to 150 m/s (outermost). The phase velocity range of 0–20 m/s is shaded in blue as spectral power in this region may be contaminated by the apparent movement of the Milky Way galaxy within the field of view of the AMTM during observations. A strong AGW activity, with phase velocities of 20–50 m/s in the northeastward direction, is clearly visible on this day.

background mean flow (Booker & Bretherton, 1967; Fritts & Alexander, 2003; Fritts & Geller, 1976; Hines & Reddy, 1967; Taylor et al., 1993). To investigate this aspect of AGW variability in our study, we generated wind-blocking diagrams using ERA5 wind data based on the principle of critical-level filtering. The relationship between the intrinsic frequency ($\hat{\omega}$) and the ground-based frequency (ω) for AGWs is given by

$$\hat{\omega} = \omega\left(1 - \frac{U_z \cos\phi + U_m \sin\phi}{c}\right) \quad (2)$$

Here, U_z and U_m are the zonal and meridional components of the background winds, respectively, whereas c and ϕ represent the phase speed and propagation direction of the wave. The propagation direction ϕ is defined in degrees counter-clockwise from East (i.e., $\phi = 0°$ is East, 90° is North, 180° is West, and 270° is South). Using these background winds, we can generate a contour to identify the region of the AGW spectra expected to be affected by critical-level filtering. This is determined by identifying AGWs propagating in specific directions and with particular phase speeds that satisfy the following condition:

$$c - U_z \cos\phi - U_m \sin\phi \leq 0 \quad (3)$$

These AGWs will encounter a critical level, where they are absorbed into the background flow and do not appear in the spectra observed at OH emission altitudes (Fritts & Alexander, 2003; Kogure et al., 2018; Taylor et al., 1993).

We used hourly background winds from ERA5 data set, as briefly discussed in Section 2.2, to identify regions of the AGW spectra expected to be affected by critical-level filtering. For this analysis, zonal and meridional winds were averaged within a ±5° latitude and longitude region around ALOMAR for the 0–50 km altitude range. For each day, these winds corresponding to the time ranges of contamination-free OH intensity maps (as shown in Figure 2), which were used to obtain AGW spectra, were temporally averaged. The altitude profiles of the resulting daily averaged zonal (red) and meridional (blue) winds from ERA5 for 05–06 January 2016 are shown in Figure 4a with their standard deviations represented by gray shaded regions. Positive values indicate northward and eastward winds for the meridional and zonal components, respectively.

These winds obtained from the ERA5 data set were used in Equation 3 to identify the set of AGWs expected to be filtered at each altitude. Such filtered regions of the AGW spectra for 05–06 January 2016 are illustrated by the white dashed contours in Figure 4b. These individual contours were combined to illustrate the overall effect of critical-level filtering between 0 and 50 km represented by the cyan contour. The region of the AGW phase velocity spectrum enclosed by this cyan contour is referred to as the forbidden (or blocked) region. The AGW spectra overlaid with these contours are termed wind-blocking diagrams. These diagrams indicate that AGWs falling within the forbidden region would not reach higher altitudes if generated below 50 km. The wind-blocking analysis presented here implicitly assumes that AGWs may originate from altitudes as low as the surface (0 km). Although the true source heights of the observed non-zero phase speed waves are unknown, starting the analysis from 0 km provides a comprehensive estimate of critical-level filtering. This ensures that any potential filtering effects throughout the entire troposphere and lower stratosphere are captured. Additionally, the interpretation relies on the assumption that the AGWs observed in the OH images taken by the ALOMAR AMTM propagated vertically within a horizontal plane extending ±5° in both latitude and longitude centered over the ALOMAR observatory. Given the unreliability at higher altitudes and significant deviation of ERA5 winds when combined with winds above 80 km from meteor radar measurements, our wind-blocking analyses were restricted to the 0–50 km altitude range. This approach allowed us to indirectly determine whether the AGWs observed in the MLT region originated from below 50 km.

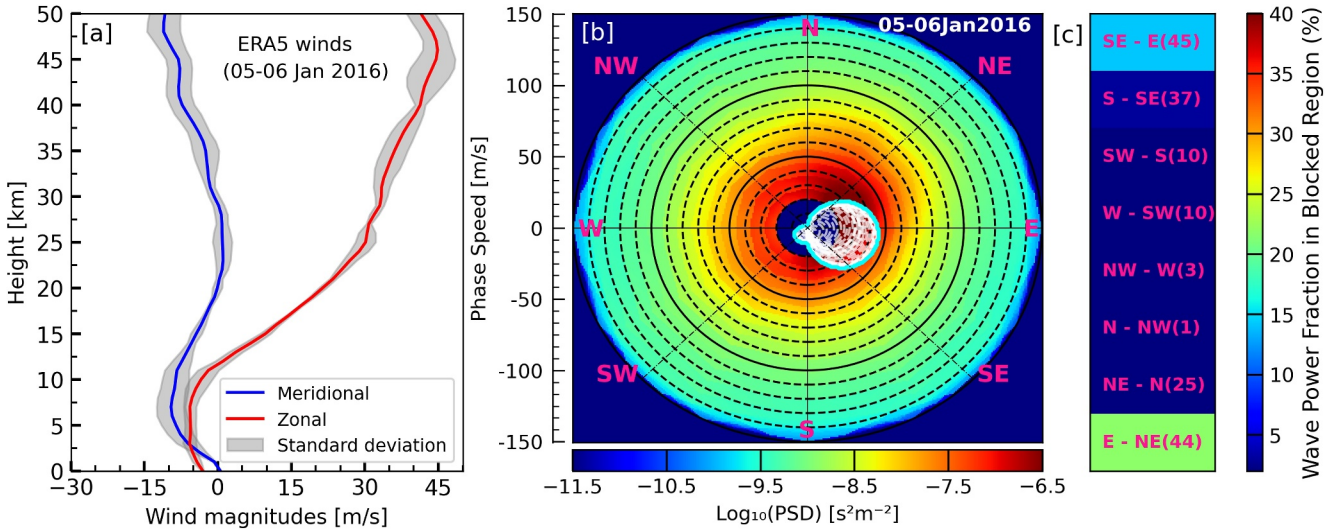

Figure 4. Illustration of the forbidden region in the atmospheric gravity wave (AGW) spectra based on critical-level filtering by background winds. (a) Altitude profiles of horizontal winds from ERA5 in zonal (red) and meridional (blue) directions for the 0–50 km altitude range, averaged over the duration of the AMTM observation on 05–06 January 2016. Shaded regions indicate the standard deviation. (b) AGW spectra (same as in Figure 3) overlaid with the calculated forbidden regions (white contours) determined at each altitude using winds shown in panel (a). The cyan contour outlines the combined forbidden region of the spectrum expected to be affected by critical-level filtering over the entire altitude range (0–50 km). (c) Percentage fraction of wave power within the blocked region (cyan contour) as a function of propagation direction. Bracketed integer values indicate the maximum wave phase speeds expected to be filtered from the observed spectra.

To further quantify the impact of critical-level filtering on the variability observed in the AGW spectra during this period, we decomposed the AGW spectra into eight directional bins: 0°–45° (E–NE), 46°–90° (NE–N), 91°–135° (N–NW), 136°–180° (NW–W), 181°–225° (W–SW), 226°–270° (SW–S), 271°–315° (S–SE), and 316°–359° (SE–E). We then calculated the percentage of total wave power inside the blocked region for each of these directional bins using:

$$P_{\text{blocked}}(\phi) = \frac{\sum_{\text{blocked}} PSD(c,\phi)}{\sum_{\text{all } c,\ \text{all } \phi} PSD(c,\phi)} \times 100 \tag{4}$$

Here, $P_{\text{blocked}}(\phi)$ denotes the percentage of wave power blocked for each propagation direction ϕ considering only AGWs inside the forbidden region. These values for 05–06 January 2016 are shown as a color map in Figure 4c, with bracketed integer values representing the maximum wave phase speeds expected to be filtered in each directional bin. Ideally, directional bins subject to strong critical-level filtering (the blocked region) should exhibit minimal wave power at OH emission altitudes. However, Figure 4c reveals slightly brighter areas (indicating ~15% wave power) primarily in the E–NE and, to some extent, SE–E directions. This suggests that not all waves observed within these two directional bins were strictly filtered out potentially due to wave sources outside the assumed vertical propagation column, waves generated above 50 km, or waves reaching the field of view through ducted propagation. This color map thus provides a clear visualization of both the strength and directional variability of critical-level filtering.

4. Results

4.1. Day-to-Day Variability of AGW Activity

4.1.1. Variability in Phase Speeds

We observed strong variability in both the individual phase velocity spectra obtained from different continuous time series of OH intensity maps and in the daily averaged spectra derived by combining them. This variability highlights both intraday and day-to-day changes in AGW activity during these periods. To further characterize this variability, we calculated spectral power in different phase speed ranges and propagation directions from the daily averaged phase velocity spectra of AGWs. As discussed earlier in Section 3.2, we excluded the PSD values

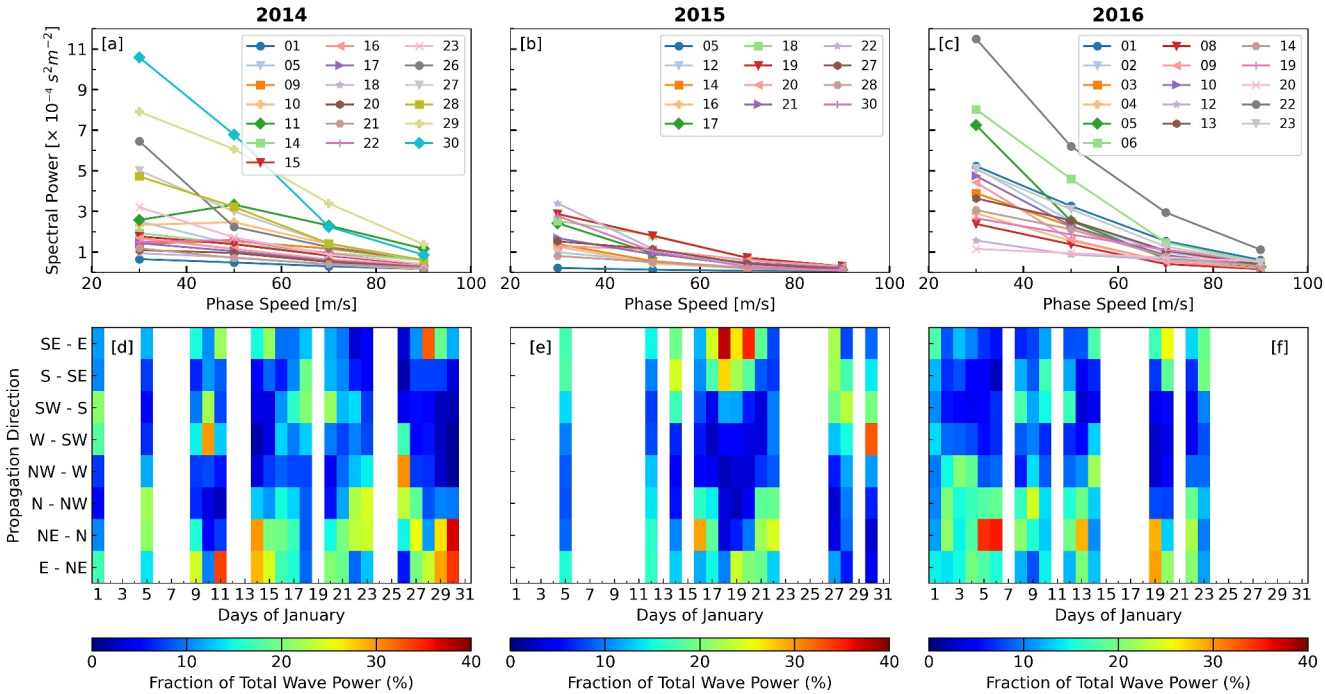

Figure 5. Day-to-day variability in the atmospheric gravity wave (AGW) spectra derived using the M-transform from OH images collected in January of 2014, 2015, and 2016. The top panels (a), (b), and (c) show spectral power variations across different wave phase speed ranges for each observation day in 2014, 2015, and 2016, respectively. Noticeably, spectral power values for AGWs in January 2015 are substantially lower compared to those observed in January 2014 and 2016. The bottom panels (d), (e), and (f) illustrate the percentage fraction of the total spectral power across different propagation directions for the corresponding days in 2014, 2015, and 2016.

in the 0–20 m/s region of the spectra from our analyses to avoid galactic contamination. Additionally, PSD values beyond phase speeds of 100 m/s (the second solid circle in Figure 3) were not considered, as the spectral power in this region is very small as evident from the logarithmic color scale in Figure 3.

We categorized each daily averaged spectrum into four phase speed ranges: 20–40, 40–60, 60–80, and 80–100 m/s to enable a detailed characterization of the AGWs observed on these days. For each of these phase speed ranges, all the PSD values within the eight quadrants (representing the propagation directions of the waves) of the phase velocity spectra were summed resulting in the total spectral power for AGWs within these speed ranges. The variation in these summed spectral powers across the defined phase speed ranges is shown in Figures 5a–5c. These values are placed at 30, 50, 70, and 90 m/s positions on the *X*-axis, corresponding to the center of the respective phase speed ranges for which the spectral powers were summed. These values obtained for all the daily averaged spectra for different days in January are represented by different colors and symbols separately for 2014, 2015, and 2016 in the top panels of Figure 5. Across all these days, higher spectral powers are consistently observed for gravity waves with propagation speeds between 20 and 40 m/s, which suggests that the majority of the observed waves are propagating within this speed range. Specifically, the maximum spectral powers of 10.6×10^{-4}, 3.4×10^{-4}, and 11.5×10^{-4} $s^2\ m^{-2}$ are observed on January 30th throughout, 22nd, and 22nd in 2014, 2015, and 2016, respectively. Similarly, the minimum powers in these three winters with values of 0.7×10^{-4}, 0.2×10^{-4}, and 1.1×10^{-4} $s^2\ m^{-2}$ were observed for AGWs with high phase speeds between 80 and 100 m/s on January 5th, 1st and 20th, respectively. This indicates that day-to-day variability within each winter is substantial and likely influenced by short-term changes in atmospheric conditions or wave source characteristics.

4.1.2. Variability in Propagation Directions

To investigate the variability in propagation directions of these AGWs, we decomposed daily averaged AGW spectra into eight directional bins as defined in Section 3.3. The spectral power for each directional bin was then summed and normalized as a percentage of the total power of the phase velocity spectra. These normalized values

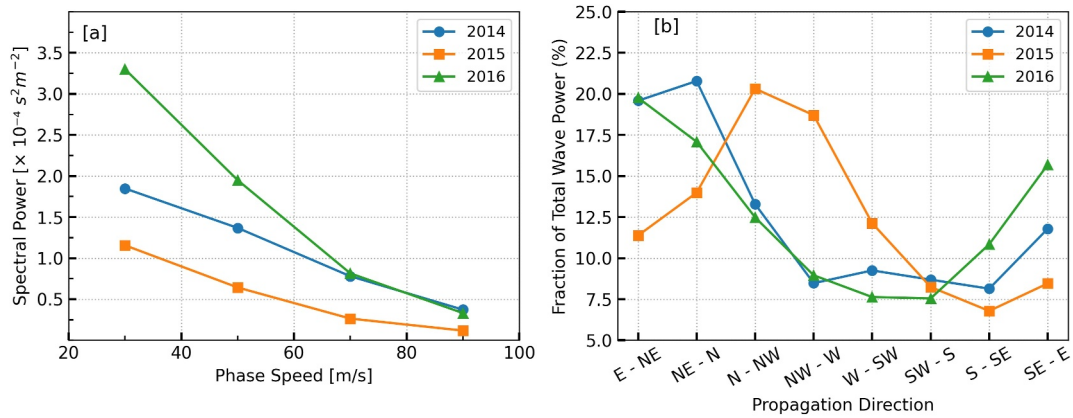

Figure 6. Year-to-year variability in atmospheric gravity wave (AGW) spectral power and propagation direction for January 2014, 2015, and 2016. (a) Mean spectral power of AGWs as a function of phase speed averaged over all days in January for each year. (b) Mean fraction of total spectral power for AGWs propagating in different directions averaged over all days in January. In 2014 and 2016, AGW propagation was predominantly in the northeast-to-north (NE–N) and east-to-northeast (E–NE) directions, respectively, whereas in 2015, the power distribution was more concentrated in the north-to-west (N–NW and NW–W) directions.

are presented as color maps in Figure 5 (bottom panels: (d), (e), (f)) with propagation directions shown along the *Y*-axis and the days of January along the *X*-axis. Figure 5d shows that AGWs in January 2014 exhibited a broad range of propagation directions with a dominant east-to-northward trend. Specifically, E–NE propagation was observed on 9, 11, 14, 15, and 28–30 January, whereas NE–N propagation occurred on 14, 22, 23, 27, 29, and 30 January. Additionally, SE–E propagation was noticeable on 28–29 January, whereas north-westward propagating waves were present on 5, 10, and 22–27 January. In contrast, AGWs in January 2015 (5e) showed more restricted propagation compared to 2014, predominantly in the south-east direction. SE–E propagation was dominant on 17–21 January and S–SE propagation during 14 and 18–20 January. South-westward propagation was observed on 27–30 January, whereas north-westward propagation occurred on 16–17 and 21–22 January. Figure 5f reveals that AGWs in January 2016 propagated mostly in the north-eastward direction with NE–N propagation particularly strong on 5–7, 13, 19, 22 January, whereas E–NE waves were observed on 13 and 19–22 January. SE–E propagation occurred on 1, 14, 19–20, and 23 January.

These results demonstrate the substantial day-to-day variability in AGW activity and propagation directions during wintertime in the high-latitude MLT region.

4.2. Year-to-Year Variability of AGW Activity

Although the day-to-day analysis in previous Section 4.1 revealed substantial variability in AGW activity within each winter, it is equally important to assess how the spectral power and propagation characteristics varied across these three winters. To quantify average year-to-year variability, we computed the averaged spectral power of AGWs within different phase speed ranges and propagation directions for each winter period. The results, shown in Figure 6, highlight distinct year-to-year differences.

Figure 6a presents the mean spectral power as a function of phase speed for January 2014 (blue), 2015 (orange), and 2016 (green). The results indicate that AGWs in 2015 consistently exhibited lower spectral power across all phase speed ranges confirming the reduced AGW activity observed in the day-to-day analysis. In contrast, AGWs in 2016 displayed the highest spectral power values, particularly for lower phase speeds (20–40 m/s), suggesting stronger wave activity compared to the other years. The spectral power for 2014 remained intermediate between these two extremes but still significantly higher than in 2015. Both the maximum and minimum spectral powers of AGWs in January 2015 were approximately two to three times lower than those observed in 2014 and 2016. Additionally, spectral power in all three years decreased with increasing phase speed, indicating that lower-speed AGWs (20–40 m/s) dominated the observed wave activity.

Figure 6b shows the mean fraction of total wave power in different propagation directions for the 3 years. A clear trend emerges, indicating that AGWs in 2014 and 2016 predominantly propagated toward the northeast (E–NE

and NE–N) directions, whereas in 2015, the power distribution was more concentrated in the north-to-west sectors (N–NW and NW–W) with a relative suppression of wave power in the northeastward sector, contrasting the patterns seen in 2014 and 2016. Notably, a secondary enhancement in wave power is observed in the southeast-to-east (SE–E) direction in all three years. This enhanced wave activity in the SE–E direction is strongest in 2016 and weakest in 2015. These differences further support the observation that AGW activity in 2015 was relatively weaker and more directionally constrained compared to 2014 and 2016.

These interannual differences in AGW spectral power and propagation directions suggest that large scale atmospheric conditions, such as differences in background wind structures and filtering effects, played a crucial role in modulating the observed wave activity. The particularly low AGW activity in 2015 may be linked to enhanced filtering in the lower atmosphere restricting the propagation of waves to the MLT region.

4.3. Intraday Variability of AGW Activity

The contrast in both spectral power and propagation directions of AGWs observed in 2015, as compared to 2014 and 2016, motivated us to examine intraday variability in greater detail. For this analysis, we applied the M-transform differently, using it on blocks of 90 consecutive perturbation images, which correspond to continuous data for one hour. These blocks were then shifted by 45 images (equivalent to 30 min) between successive analyses. This approach enabled us to obtain AGW phase velocity spectra at 30-min intervals throughout the duration of available good images each day providing insight into the variability of gravity wave activity within each day.

To quantify AGW activity at different times of the day, we summed the spectral power of AGW spectra with phase speeds between 20–100 m/s. These total spectral power values, obtained from each AGW spectrum at 30-min intervals, are shown as a function of time in Figure 7a for 2014, (b) for 2015, and (c) for 2016 with each day represented by different colors and symbols. The results reveal significantly less variation in the spectral power of AGWs across the observation period throughout the day in 2015 compared to 2014 and 2016. Additionally, consistent with Figure 5, the maximum values of total spectral power for AGWs at different times of the day in 2015 are lower than those in 2014 and 2016. In 2014, strong variability in AGW activity, characterized by higher spectral power, is particularly evident between 26 and 30 January. Conversely, in 2016, significant variability in the spectral power of AGWs is present almost every day.

The intraday variability results further confirm that AGW activity exhibits significant variations within individual days with notable differences between years.

5. Discussion

The detailed analyses of AGW phase velocity spectra obtained during January 2014, 2015, and 2016, as presented in the previous sections, reveal significant variability. Notably, AGW activity in 2015 was considerably lower with reduced spectral power (Figures 5a–5c and 6a) and distinct changes in propagation directions (Figures 5d–5f and 6b) compared to 2014 and 2016. In our study, most AGWs in the MLT region propagated eastward (northeastward and southeastward) during this period except for 2015 when strong wave activity in the northwestward direction was also observed as illustrated in Figures 5d–5f and 6b. The southeastward and northwestward propagating AGWs observed on 14th January 2016 are consistent with the flight-based measurements near ALOMAR by Wüst et al. (2019).

Other high-latitude studies of gravity waves in the mesosphere have identified a range of sources for variability. Using OH image observations from Resolute Bay, Canada (74.7°N, 265.1°E), Suzuki et al. (2009) and J. Li et al. (2020) reported that most mesospheric AGWs observed during Arctic winter months propagated westward with phase speeds between 30 and 60 m/s. This preferential propagation direction was attributed to critical-level filtering by winds in the lower and middle atmosphere. In contrast, northeastward propagating mesospheric AGWs with phase speeds 20–70 m/s have been observed over Kazan (55.8°N, 49.2°E) and Tunkinskaya (51°N, 103°E) in Russia (Q. Li et al., 2018; Tashchilin et al., 2010). Both Suzuki et al. (2009) and Q. Li et al. (2018) showed that the majority of the AGWs were observed during periods of enhanced tropospheric activity, including tropospheric updrafts associated with low-pressure systems near Resolute Bay and deep convection and strong jet streams over Kazan. Several other studies have highlighted that stratospheric wind structures play a key role in modulating AGW variability in the MLT region. This includes changes in gravity wave momentum flux in the

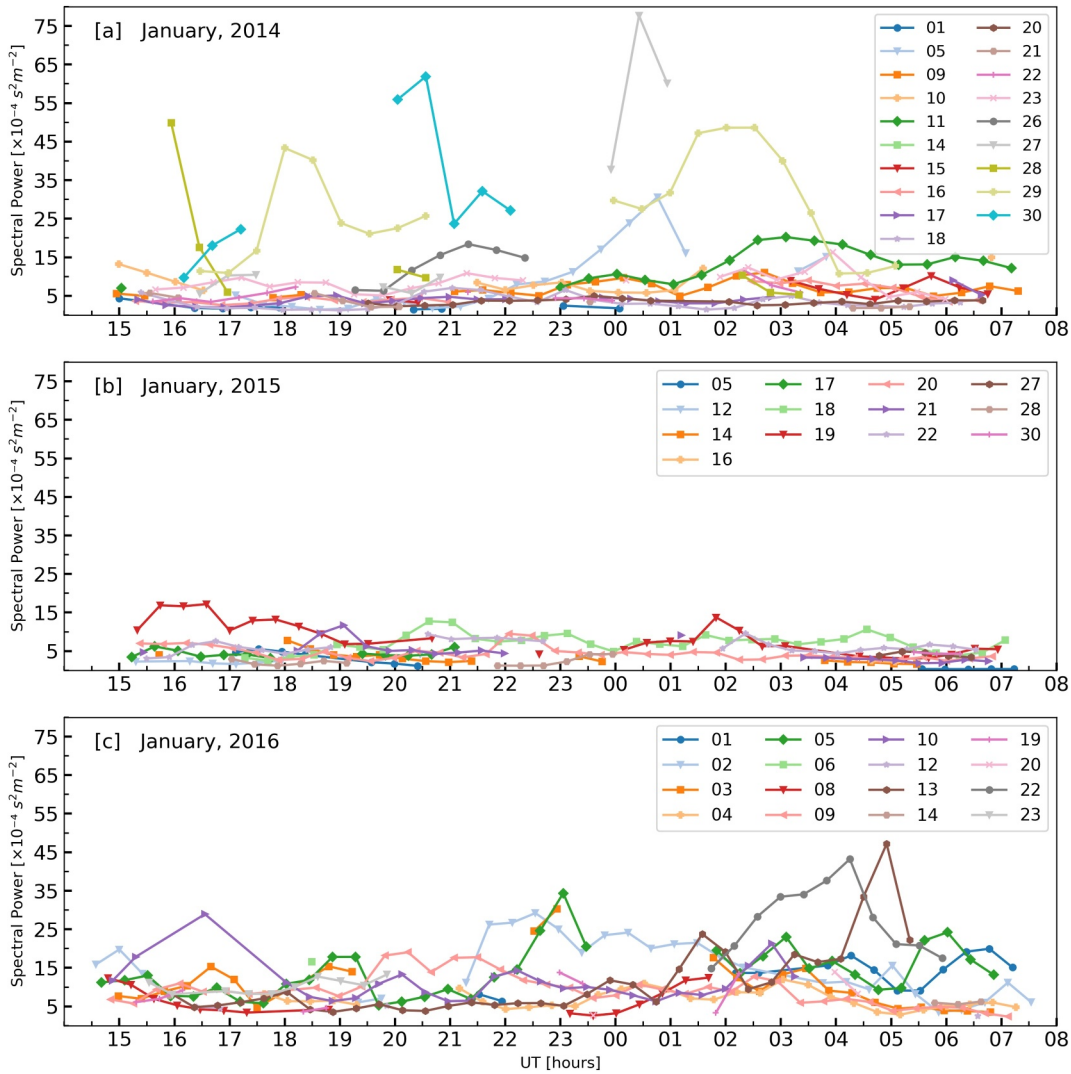

Figure 7. Intraday variability in atmospheric gravity wave (AGW) spectra obtained using the M-transform for January 2014, 2015, and 2016. The total spectral power for AGWs with phase speeds in the range 20–100 m/s is plotted as a function of time of day for each individual day represented by different colors and symbols in panel (a) for 2014, (b) for 2015, and (c) for 2016.

high-latitudes of the Northern Hemisphere (Matthias et al., 2012; Thurairajah et al., 2010), seasonal variations in AGW propagation directions in the mid-latitudes (Nakamura et al., 1999) and variability in AGW spectra over Antarctica (Kam et al., 2021; Kogure et al., 2018; Matsuda et al., 2017). Notably, these studies found strongest spectral powers are associated with AGWs propagating at phase speeds below 60 m/s, which is similar to our results in Figures 5a–5c, where the highest spectral powers are observed for gravity waves propagating at speeds between 20 and 40 m/s. Additionally, studies in the Antarctic region revealed that gravity waves with phase speeds below 60 m/s predominantly propagate westward, whereas those with phase speeds exceeding 80 m/s tend to propagate eastward. This disparity in propagation directions was attributed to critical-level filtering by stratospheric winds (Matsuda et al., 2017).

To examine the impact of local wind conditions on AGW activity observed at ALOMAR, we analyzed the directional blocking of AGWs due to critical-level filtering by background winds within the 0–50 km altitude range. To investigate the connection between variations in AGW activity and stratospheric conditions, we utilized the Arctic Oscillation (AO) index as an indicator of the polar vortex strength in the Northern Hemisphere as discussed in Section 2.3.

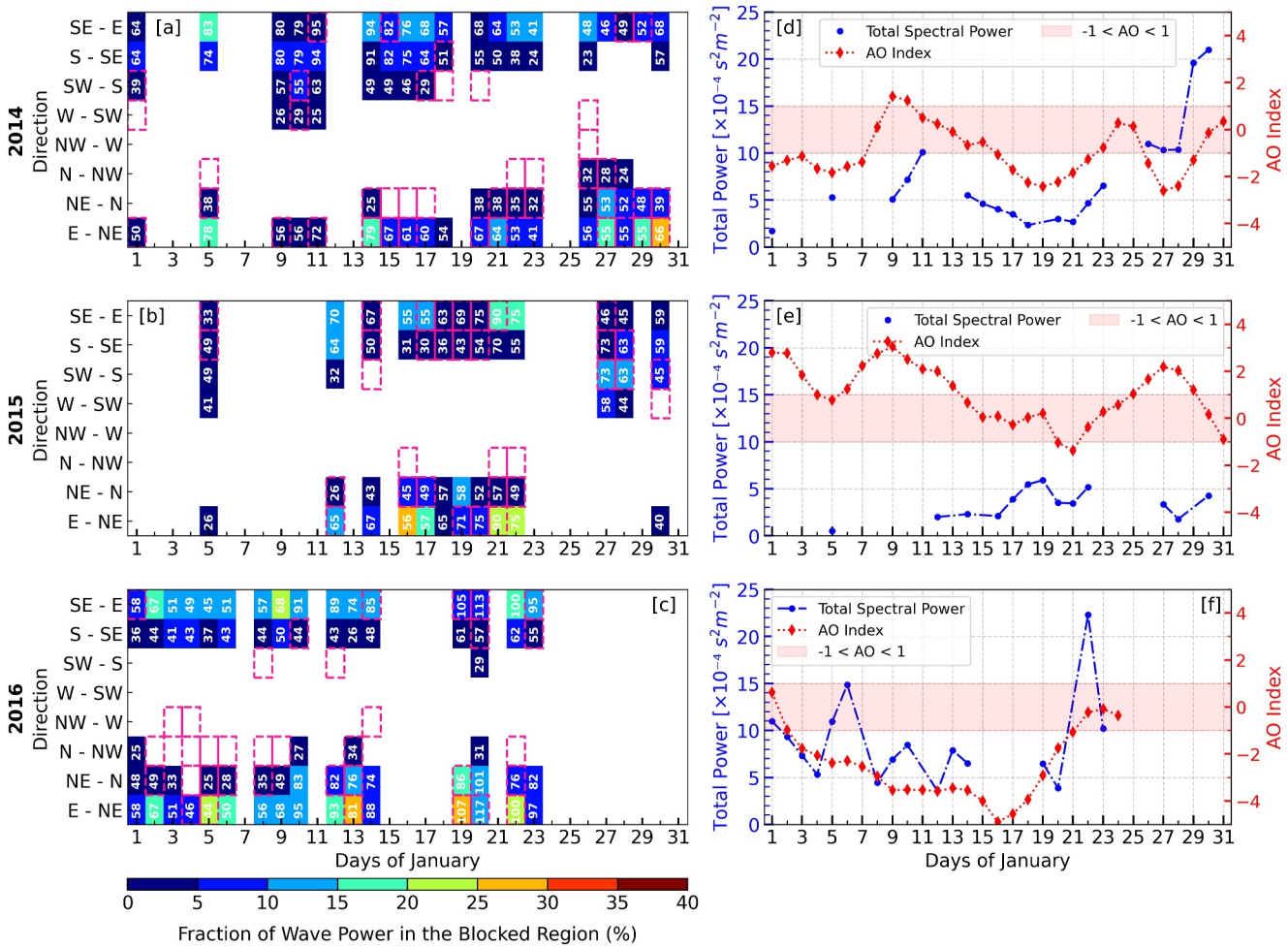

Figure 8. Day-to-day variability in the strength of critical-level filtering (left panels) and the comparison of atmospheric gravity wave (AGW) spectral power with the Arctic Oscillation (AO) index (right panels) for January 2014, 2015, and 2016. (a) The fraction of wave power inside the blocked region for different propagation directions on each day of January for 2014. This panel is similar to Figure 4c but now includes the maximum phase speed values expected to be filtered in each directional bin, overlaid in each grid cell. Additionally, red dashed borders highlight the dominant wave propagation directions on each day, corresponding to the propagation directions showing stronger wave activity (brighter bins) in Figure 5d. (b) and (c) Same as panel (a) but for 2015 and 2016, respectively. Empty grid cells indicate that no effective directional filtering of AGWs was taking place. (d)–(f) Comparison between the total spectral power of AGWs (blue circles) and the AO index (red diamonds) for (d) 2014, (e) 2015, and (f) 2016. The red-shaded region represents the AO index within the range of ±1.

Figure 8 panels (a) to (c) illustrate the day-to-day variability in the strength of critical-level filtering for January of 2014, 2015, and 2016, respectively. The fractions of wave power within the blocked regions for each directional bin were derived using Equation 4 (as discussed in Section 3.3). The numbers overlaid within each grid cell indicate the maximum wave phase speeds expected to be filtered in these directional bins due to critical-level filtering by winds below 50 km altitude. Empty grid cells in these color maps correspond to cases where either the maximum possible filtered phase speed was below 20 m/s, or the background winds were not oriented to enable blocking in that direction on that day. As such, these empty grid cells indicate that no directional filtering of AGWs was taking place. Red dashed borders are used in panels (a–c) to highlight the dominant AGW propagation directions on each day, corresponding to the directional bins exhibiting enhanced spectral power (brighter shading) in Figures 5d–5f. Figures 8d–8f compare the total spectral power (integrated over phase speed ranges of 20–100 m/s) of daily averaged M-transform outputs (blue circles) with the Arctic Oscillation (AO) index (red diamonds) for January of 2014, 2015, and 2016, respectively. The red-shaded regions indicate the AO index within the range of ±1. The variability in daily total spectral power corresponds to the day-to-day, year-to-year, and intraday changes across the three winters as depicted in Figures 5–7.

As discussed in Section 3.3, critical-level filtering plays a key role in determining which AGWs can propagate to mesospheric altitudes. If the observed waves were generated below 50 km, then directional bins experiencing strong filtering should exhibit minimal AGW spectral power at OH altitudes, as these waves would have been absorbed by the background wind field before reaching the upper mesosphere. The darker colors (values below 15%) and the empty cells observed in most directional bins across the three winters (Figures 8a–8c) indicate that the majority of AGWs reaching MLT altitudes during this period originated from below 50 km, consistent with previous reports from Resolute Bay and Kazan (Li et al., 2018; Suzuki et al., 2009). The red dashed borders in Figures 8a–8c highlight the directional bins with strong AGW activity observed in the OH images, providing a direct visual correspondence between low directional filtering fractions and enhanced wave power. For example, in 2014 (Figure 8a), strong AGW activity was observed on 1, 5, 9–11, 14–16, 18–23, and 26–30 January, most of which coincide with directional bins that have low (<15%) or no effective filtering. A similar correspondence is seen in 2015 (Figure 8b), where enhanced wave activity on 5, 14, 16–22, 27–28, and 30 January aligns with relatively low directional filtering fractions or empty grid cells. For 2016, most of the red highlighted directional bins with strong AGW activity also coincide with bins exhibiting low or no directional filtering (Figure 8c). Except for a very few directional bins, this consistent one-to-one correspondence across multiple days and years strongly suggests that the AGWs observed in the OH images were significantly influenced by critical-level filtering by winds between 0 and 50 km.

On certain days, one or more directional bins displayed brighter colors (values exceeding 15%) occurring on 5 out of 19 days in 2014, 4 out of 13 days in 2015, and 8 out of 16 days during 2016. These instances suggest that not all waves in these directional bins were strictly filtered out. This could be due to (a) waves originating outside the assumed vertical propagation column within the ±5° latitude and longitude region surrounding ALOMAR (Bossert et al., 2014), (b) waves generated at altitudes above 50 km or secondary waves generated from wave breaking or other nonlinear processes (Bossert et al., 2017; Kogure et al., 2020; Vadas et al., 2023), where the applied wind-blocking analysis is no longer valid, and (c) waves that reached the instrument's field of view from more distant regions via ducted propagation (Z. Li et al., 2011; Q. Li et al., 2016; J. Li et al., 2020; Wrasse et al., 2024).

In addition to critical-level filtering, the observed directional asymmetry in AGW spectral power may also be influenced by Doppler shifting and subsequent wave cancellation effects within the OH emission layer, particularly when vertical wavelengths are shorter than the OH layer thickness, thereby reducing AGW visibility. AGWs, propagating in an environment where the difference between the phase speed and the background wind increases, are Doppler shifted to longer vertical wavelengths, which are less susceptible to cancellation, and therefore more readily detectable in airglow images. In contrast, AGWs propagating with the background wind may exhibit shorter vertical wavelengths, increasing the likelihood of partial or complete cancellation within the airglow emission layer. This observational bias can further influence the distribution of wave power in different directions (Z. Li et al., 2011; Liu & Swenson, 2003). Additionally, AGWs can undergo reflection at a turning level when their intrinsic frequency equals the buoyancy frequency, resulting in a zero vertical wavenumber (Fritts & Alexander, 2003; Tomikawa, 2015).

The higher number of days with wave power in blocked directional bins exceeding 15% in 2016 could be a contributing factor to the higher AGW spectral power observed in Figures 6a and 8f, as a larger fraction of AGW energy may have reached MLT altitudes in this period, leading to the enhanced wave activity observed that year. In contrast, the distinctly lower AGW spectral power and constrained propagation directions observed in 2015 (Figures 5 and 6) compared to 2014 and 2016 suggest the need for further analysis to assess the role of large-scale atmospheric conditions, if any, in addition to local wind filtering.

We used the AO index values at 1,000 hPa to represent high-latitude stratospheric conditions with AO >1 and AO < −1 indicating strong and weak polar vortex scenarios, respectively (Baldwin & Dunkerton, 1999). The AO index values for January in these 3 years are displayed in Figures 8d–8f with the ranges between ±1 shown as red shaded regions. In 2015, the AO index was generally higher compared to 2014 and 2016. A stronger polar vortex, indicated by positive AO index values, is associated with intensified eastward zonal winds in the upper stratosphere of high-latitudes (Andrews et al., 1987; Labitzke, 1972; Matsuno, 1971). These strong eastward winds were expected to filter eastward-propagating AGWs originating from lower altitudes leading to reduced overall AGW activity in the MLT region. This is evident in the phase velocity spectra from January 2015 which show lower spectral powers (Figures 5b, 6a, 7b, and 8e). However, Figure 6b also shows that AGW propagation

directions in 2015 were distinct compared to 2014 and 2016 with a greater fraction of waves propagating northwestward instead of predominantly eastward. This further confirms the influence of the strong polar vortex in 2015, which not only suppressed overall AGW activity but also altered the preferred propagation directions, likely due to enhanced filtering of eastward-propagating waves. Additionally, during 17–21 January 2015, AGW activity was notably stronger in the eastward direction, while from 27 to 30 January, spectral power was more pronounced in the southwestward direction (Figure 5e; red-dashed regions in Figure 8b). These intervals coincide with periods of lower and higher AO index values, respectively (Figure 8e). Such similarity indicates a strong influence of stratospheric winds on the gravity wave variability observed in the Arctic MLT region.

During January 2014, the relatively weak polar vortex, as indicated by frequent negative AO values (Figure 8d), allowed more gravity waves to propagate upward, resulting in increased AGW spectral power (Figures 5a, 6a, and 8d), and greater variability in gravity wave activity (Figure 7a). The strong eastward propagation of AGWs during 11, 13–16, and 27–30 January 2014 (Figure 5d and red-dashed directional bins in Figure 8a) coincides with lower values of AO index (Figure 8d). In contrast, in January 2016, the significantly lower AO values, particularly from 02 to 20 January (Figure 8f), minimized the filtering of upward propagating gravity waves in the upper stratosphere leading to a comparatively more diverse spectrum of AGWs in the OH images (Figures 5c, 5f, and 7c). The higher spectral powers for eastward-propagating gravity waves in 2016, as seen in Figure 5f (and by red-dashed directional grids in Figure 8c), further confirm the reduced wave filtering in the stratosphere due to weaker eastward winds. The periods of enhanced southeast-to-eastward (SE–E) propagation of waves particularly visible during 5, 14, 17–21, 27 January 2015, and 11, 15, and 28–29 January 2014, and 1, 14, 19–20, 23 January 2016 contribute to a consistent secondary peak observed in the annual averaged directional distributions (Figure 6b). This recurrent secondary enhancement in SE–E sectors across all 3 years is likely linked to episodic reductions in stratospheric filtering during intervals of lower AO index values. Our results for January 2015, when the polar vortex was stronger, align with those reported from Antarctica (Kam et al., 2021; Kogure et al., 2023; Matsuda et al., 2017), where strong eastward stratospheric winds were associated with reduced AGW activity. However, the spectral powers for AGWs from the winters of 2014 and 2016 in our study are several times higher than those reported for Antarctic winters likely due to differences in polar vortex strength and gravity wave sources between the Arctic and Antarctic regions. It should be noted that such a one-to-one comparison between AGW spectra obtained from our work and those reported from Antarctic regions (Kam et al., 2021; Kogure et al., 2023; Matsuda et al., 2017) is made possible because all these results were obtained using the M-transform for the same ranges of wave periods and horizontal wavelengths, highlighting the advantage of this technique. Therefore, the results presented in this work on the variability of AGWs observed in OH intensity maps demonstrate that stratospheric winds are the primary driver of the strong variability in AGW activity in the MLT region during the winters of 2014, 2015, and 2016.

6. Summary

This study presents a detailed investigation of the variability observed in short-period (<1 hr) AGWs in the high-latitude MLT region during January 2014, 2015, and 2016. We utilized OH (3,1) band emission intensity maps obtained from the ALOMAR AMTM and applied the M-transform technique to derive horizontal phase velocity spectra of the gravity waves. Our results were compared with previous mesospheric gravity wave observations from both the Arctic and Antarctic to provide a broader geophysical perspective and highlight regional similarities and differences. To address the observed AGW variability during these Arctic winter periods, we incorporated background winds from the ERA5 reanalysis data set (0–50 km altitude) and daily values of the Arctic Oscillation index as a proxy for the strength of the stratospheric polar vortex in the Northern Hemisphere. The key findings from this study are as follows:

- Spectral power distributions across different phase speeds and propagation directions showed pronounced intraday, day-to-day, and year-to-year variability.
- Gravity wave activity in 2015 was notably suppressed, exhibiting both lower spectral power and marked shifts in dominant propagation directions compared to 2014 and 2016.
- Wind-blocking diagrams, generated using ERA5 wind profiles, indicate that most AGWs observed in the MLT region during this period were likely originated from the 0–50 km altitude range.
- The interannual variability in spectral power and dominant propagation directions is likely associated with critical-level filtering of AGWs by stratospheric winds.

These findings highlight the role of stratospheric conditions in driving AGW activity and variability in the Arctic MLT region. In future work, we plan to investigate the seasonal changes and long-term trends of gravity waves in the Arctic MLT region as well as the impact of planetary waves on AGW variability. We plan to utilize 2D temperature maps obtained from ALOMAR AMTM during 2012–2017 to study the drivers of variability in temperatures of the Arctic MLT region.

Data Availability Statement

The Advanced Mesospheric Temperature Mapper (AMTM) at ALOMAR is operated and maintained by Utah State University, USA. The OH (3,1) band emission data utilized in this study were provided through a collaborative agreement. OH (3,1) band emission intensity maps for January 2014, 2015, and 2016 (Taylor & Pautet, 2024), along with detailed information about the data files, are publicly available at the UK Polar Data Center (https://data.bas.ac.uk/full-record.php?id=GB/NERC/BAS/PDC/01924). The M-transform software was provided by the National Institute of Polar Research, Japan and is available upon request from Prof. Takuji Nakamura (nakamura.takuji@nipr.ac.jp). The details about the M-transform software are available on the National Institute of Polar Research, Japan website at http://polaris.nipr.ac.jp/~airglow/M-transform/ and its application to airglow data sets is discussed by Matsuda et al. (2014) and Perwitasari et al. (2018). ERA5 reanalysis data (Hersbach et al., 2017, 2020) were obtained from the Copernicus Climate Data Store (CDS) and downloaded on model levels using the CDS API. ERA5 data are accessible at https://cds.climate.copernicus.eu/datasets/reanalysis-era5-complete?tab=overview. Daily values of the Arctic Oscillation (AO) index are obtained from the National Weather Service Climate Prediction Center (CPC) at (https://ftp.cpc.ncep.noaa.gov/cwlinks/).

Acknowledgments
This work is part of the MesoS2D (Mesospheric sub-seasonal to decadal predictability) project (https://www.bas.ac.uk/project/mesos2d/), which aims to characterize the drivers of variability in the mesosphere-lower-thermosphere/ionosphere with the ultimate goal of identifying pathways to improving our capability of forecasting this region. Subir Mandal and Tracy Moffat-Griffin are funded through the MesoS2D Grant (NERC Reference:NE/V018426/1) for this work. Corwin J. Wright is funded by the Royal Society Fellowship (URF\R\221023) and NERC Grants (NE/V01837X/1 and NE/W003201/1). The AMTM operations at ALOMAR were supported under an NSF collaborative Grant AGS-1042227.

References

Alexander, M. J., Beres, J. H., & Pfister, L. (2000). Tropical stratospheric gravity wave activity and relationships to clouds. *Journal of Geophysical Research*, *105*(D17), 22299–22309. https://doi.org/10.1029/2000jd900326

Alexander, M. J., & Pfister, L. (1995). Gravity wave momentum flux in the lower stratosphere over convection. *Geophysical Research Letters*, *22*(15), 2029–2032. https://doi.org/10.1029/95gl01984

Alexander, M. J., & Teitelbaum, H. (2007). Observation and analysis of a large amplitude mountain wave event over the Antarctic Peninsula. *Journal of Geophysical Research*, *112*(D21). https://doi.org/10.1029/2006jd008368

Alexander, S., Klekociuk, A., & Murphy, D. (2011). Rayleigh Lidar observations of gravity wave activity in the winter upper stratosphere and lower mesosphere above Davis, Antarctica (69 s, 78 e). *Journal of Geophysical Research*, *116*(D13), D13109. https://doi.org/10.1029/2010jd015164

Andrews, D. G., Holton, J. R., & Leovy, C. B. (1987). *Middle atmosphere dynamics (No. 40)*. Academic Press. https://doi.org/10.1038/294519a0

Baker, D. J., & Stair, A., Jr. (1988). Rocket measurements of the altitude distributions of the hydroxyl airglow. *Physica Scripta*, *37*(4), 611–622. https://doi.org/10.1088/0031-8949/37/4/021

Baldwin, M. P., & Dunkerton, T. J. (1999). Propagation of the arctic oscillation from the stratosphere to the troposphere. *Journal of Geophysical Research*, *104*(D24), 30937–30946. https://doi.org/10.1029/1999jd900445

Becker, E. (2012). Dynamical control of the middle atmosphere. *Space Science Reviews*, *168*(1–4), 283–314. https://doi.org/10.1007/s11214-011-9841-5

Booker, J. R., & Bretherton, F. P. (1967). The critical layer for internal gravity waves in a shear flow. *Journal of Fluid Mechanics*, *27*(3), 513–539. https://doi.org/10.1017/s0022112067000515

Bossert, K., Fritts, D. C., Pautet, P.-D., Taylor, M. J., Williams, B. P., & Pendelton, W. R. (2014). Investigation of a mesospheric gravity wave ducting event using coordinated sodium Lidar and mesospheric temperature mapper measurements at Alomar, Norway (69 n). *Journal of Geophysical Research: Atmospheres*, *119*(16), 9765–9778. https://doi.org/10.1002/2014jd021460

Bossert, K., Kruse, C. G., Heale, C. J., Fritts, D. C., Williams, B. P., Snively, J. B., et al. (2017). Secondary gravity wave generation over New Zealand during the deepwave campaign. *Journal of Geophysical Research: Atmospheres*, *122*(15), 7834–7850. https://doi.org/10.1002/2016jd026079

Coble, M., Papen, G. C., & Gardner, C. S. (1998). Computing two-dimensional unambiguous horizontal wavenumber spectra from oh airglow images. *IEEE Transactions on Geoscience and Remote Sensing*, *36*(2), 368–382. https://doi.org/10.1109/36.662723

Espy, P. J., Jones, G. O. L., Swenson, G. R., Tang, J., & Taylor, M. J. (2004). Seasonal variations of the gravity wave momentum flux in the antarctic mesosphere and lower thermosphere. *Journal of Geophysical Research*, *109*(D23). https://doi.org/10.1029/2003JD004446

Fritts, D. C. (1982). Shear excitation of atmospheric gravity waves. *Journal of the Atmospheric Sciences*, *39*(9), 1936–1952. https://doi.org/10.1175/1520-0469(1982)039⟨1936:seoagw⟩2.0.co;2

Fritts, D. C. (1984). Shear excitation of atmospheric gravity waves. Part ii: Nonlinear radiation from a free shear layer. *Journal of the Atmospheric Sciences*, *41*(4), 524–537. https://doi.org/10.1175/1520-0469(1984)041⟨0524:seoagw⟩2.0.co;2

Fritts, D. C., & Alexander, M. J. (2003). Gravity wave dynamics and effects in the middle atmosphere. *Reviews of Geophysics*, *41*(1). https://doi.org/10.1029/2001RG000106

Fritts, D. C., Baumgarten, G., Pautet, P.-D., Hecht, J. H., Williams, B. P., Kaifler, N., et al. (2023). Kelvin–Helmholtz instability "tube" and "knot" dynamics. Part I: Expanding observational evidence of occurrence and environmental influences. *Journal of the Atmospheric Sciences*, *80*(10), 2419–2437. https://doi.org/10.1175/jas-d-22-0189.1

Fritts, D. C., & Geller, M. A. (1976). Viscous stabilization of gravity wave critical level flows. *Journal of the Atmospheric Sciences*, *33*(12), 2276–2284. https://doi.org/10.1175/1520-0469(1976)033⟨2276:vsogwc⟩2.0.co;2

Fritts, D. C., Pautet, P.-D., Bossert, K., Taylor, M. J., Williams, B. P., Iimura, H., et al. (2014). Quantifying gravity wave momentum fluxes with mesosphere temperature mappers and correlative instrumentation. *Journal of Geophysical Research: Atmospheres*, *119*(24), 13–583. https://doi.org/10.1002/2014jd022150

Fritts, D. C., Smith, R. B., Taylor, M. J., Doyle, J. D., Eckermann, S. D., Dörnbrack, A., et al. (2016). The deep propagating gravity wave experiment (DEEPWAVE): An airborne and ground-based exploration of gravity wave propagation and effects from their sources throughout the lower and middle atmosphere. *Bulletin of the American Meteorological Society*, *97*(3), 425–453. https://doi.org/10.1175/bams-d-14-00269.1

Fritts, D. C., & Vanzandt, T. E. (1993). Spectral estimates of gravity wave energy and momentum fluxes. Part I: Energy dissipation, acceleration, and constraints. *Journal of the Atmospheric Sciences*, *50*(22), 3685–3694. https://doi.org/10.1175/1520-0469(1993)050(3685:seogwe)2.0.co;2

Garcia, F., Taylor, M. J., & Kelley, M. (1997). Two-dimensional spectral analysis of mesospheric airglow image data. *Applied Optics*, *36*(29), 7374–7385. https://doi.org/10.1364/ao.36.007374

Gardner, C. S. (1991). Introduction to aloha-90: The airborne Lidar and observations of the Hawaiian airglow campaign. *Geophysical Research Letters*, *18*(7), 1313–1316. https://doi.org/10.1029/91gl01294

Goldberg, R., Fritts, D., Schmidlin, F., Williams, B., Croskey, C., Mitchell, J., et al. (2006). The Macwave program to study gravity wave influences on the polar mesosphere. In *Annales Geophysicae* (Vol. 24(4), pp. 1159–1173). https://doi.org/10.5194/angeo-24-1159-2006

Hapgood, M., & Taylor, M. J. (1982). Analysis of airglow image data. *Annales de Geophysique*, *38*, 805–813. https://doi.org/10.1364/ao.36.007374

Hecht, J. H., Walterscheid, R., & Ross, M. (1994). First measurements of the two-dimensional horizontal wave number spectrum from CCD images of the nightglow. *Journal of Geophysical Research*, *99*(A6), 11449–11460. https://doi.org/10.1029/94ja00584

Hersbach, H., Bell, B., Berrisford, P., Hirahara, S., Horányi, A., Muñoz-Sabater, J., et al. (2020). The ERA5 global reanalysis. *Quarterly Journal of the Royal Meteorological Society*, *146*(730), 1999–2049. https://doi.org/10.1002/qj.3803

Hersbach, H., Bell, B., Berrisford, P., Hirahara, S., Horányi, A., Muñoz-Sabater, J., et al. (2017). Complete ERA5 from 1940: Fifth generation of ECMWF atmospheric reanalyzes of the global climate. https://doi.org/10.24381/cds.143582cf

Hindley, N. P., Smith, N. D., Wright, C. J., Rees, D. A. S., & Mitchell, N. J. (2016). A two-dimensional stockwell transform for gravity wave analysis of airs measurements. *Atmospheric Measurement Techniques*, *9*(6), 2545–2565. https://doi.org/10.5194/amt-9-2545-2016

Hindley, N. P., Wright, C. J., Gadian, A. M., Hoffmann, L., Hughes, J. K., Jackson, D. R., et al. (2021). Stratospheric gravity waves over the mountainous island of South Georgia: Testing a high-resolution dynamical model with 3-d satellite observations and radiosondes. *Atmospheric Chemistry and Physics*, *21*(10), 7695–7722. https://doi.org/10.5194/acp-21-7695-2021

Hines, C. O., & Reddy, C. (1967). On the propagation of atmospheric gravity waves through regions of wind shear. *Journal of Geophysical Research*, *72*(3), 1015–1034. https://doi.org/10.1029/gm018p0567

Kam, H., Song, I.-S., Kim, J.-H., Kim, Y. H., Song, B.-G., Nakamura, T., et al. (2021). Mesospheric short-period gravity waves in the Antarctic Peninsula observed in all-sky airglow images and their possible source locations. *Journal of Geophysical Research: Atmospheres*, *126*(24), e2021JD035842. https://doi.org/10.1029/2021jd035842

Kogure, M., Nakamura, T., Ejiri, M. K., Nishiyama, T., Tomikawa, Y., & Tsutsumi, M. (2018). Effects of horizontal wind structure on a gravity wave event in the middle atmosphere over Syowa (69 s, 40 e), the Antarctic. *Geophysical Research Letters*, *45*(10), 5151–5157. https://doi.org/10.1029/2018gl078264

Kogure, M., Nakamura, T., Murphy, D. J., Taylor, M. J., Zhao, Y., Pautet, P.-D., et al. (2023). Characteristics of gravity wave horizontal phase velocity spectra in the mesosphere over the Antarctic stations, Syowa and Davis. *Journal of Geophysical Research: Atmospheres*, *128*(6), e2022JD037751. https://doi.org/10.1029/2022jd037751

Kogure, M., Yue, J., & Liu, H. (2021). Gravity wave weakening during the 2019 Antarctic stratospheric sudden warming. *Geophysical Research Letters*, *48*(8), e2021GL092537. https://doi.org/10.1029/2021gl092537

Kogure, M., Yue, J., Nakamura, T., Hoffmann, L., Vadas, S. L., Tomikawa, Y., et al. (2020). First direct observational evidence for secondary gravity waves generated by mountain waves over the Andes. *Geophysical Research Letters*, *47*(17), e2020GL088845. https://doi.org/10.1029/2020gl088845

Krassovsky, V., & Shagaev, M. (1977). On the nature of internal gravitational waves observed from hydroxyl emission. *Planetary and Space Science*, *25*(2), 200–201. https://doi.org/10.1016/0032-0633(77)90027-7

Labitzke, K. (1972). Temperature changes in the mesosphere and stratosphere connected with circulation changes in winter. *Journal of the Atmospheric Sciences*, *29*(4), 756–766. https://doi.org/10.1175/1520-0469(1972)029⟨0756:tcitma⟩2.0.co;2

Lanchester, B. S. (1985). *Relation between discrete auroral forms and magnetic field disturbances Doctoral dissertation*. University of Southampton. https://doi.org/10.1139/p61-033

Li, J., Li, T., Wu, Q., Tang, Y., Wu, Z., & Cui, J. (2020). Characteristics of small-scale gravity waves in the arctic winter mesosphere. *Journal of Geophysical Research: Space Physics*, *125*(6), e2019JA027643. https://doi.org/10.1029/2019ja027643

Li, Q., Xu, J., Liu, X., Yuan, W., & Chen, J. (2016). Characteristics of mesospheric gravity waves over the southeastern Tibetan Plateau region. *Journal of Geophysical Research: Space Physics*, *121*(9), 9204–9221. https://doi.org/10.1002/2016ja022823

Li, Q., Yusupov, K., Akchurin, A., Yuan, W., Liu, X., & Xu, J. (2018). First oh airglow observation of mesospheric gravity waves over European Russia region. *Journal of Geophysical Research: Space Physics*, *123*(3), 2168–2180. https://doi.org/10.1002/2017ja025081

Li, Z., Liu, A. Z., Lu, X., Swenson, G. R., & Franke, S. J. (2011). Gravity wave characteristics from oh airglow imager over Maui. *Journal of Geophysical Research*, *116*(D22). https://doi.org/10.1029/2011jd015870

Lindzen, R. S. (1981). Turbulence and stress owing to gravity wave and tidal breakdown. *Journal of Geophysical Research*, *86*(C10), 9707–9714. https://doi.org/10.1029/jc086ic10p09707

Liu, A. Z., & Swenson, G. R. (2003). A modeling study of O2 and OH airglow perturbations induced by atmospheric gravity waves. *Journal of Geophysical Research*, *108*(D4). https://doi.org/10.1029/2002jd002474

Matsuda, T. S., Nakamura, T., Ejiri, M. K., Tsutsumi, M., & Shiokawa, K. (2014). New statistical analysis of the horizontal phase velocity distribution of gravity waves observed by airglow imaging. *Journal of Geophysical Research: Atmospheres*, *119*(16), 9707–9718. https://doi.org/10.1002/2014jd021543

Matsuda, T. S., Nakamura, T., Ejiri, M. K., Tsutsumi, M., Tomikawa, Y., Taylor, M. J., et al. (2017). Characteristics of mesospheric gravity waves over Antarctica observed by Antarctic gravity wave instrument network imagers using 3-D spectral analyses. *Journal of Geophysical Research: Atmospheres*, *122*(17), 8969–8981. https://doi.org/10.1002/2016jd026217

Matsuno, T. (1971). Adynamical model of the stratospheric sudden warming. *Journal of the Atmospheric Sciences*, *28*(8), 1095–1107. https://doi.org/10.1175/1520-0469(1971)028<1479:admots>2.0.co;2

Matthias, V., Hoffmann, P., Rapp, M., & Baumgarten, G. (2012). Composite analysis of the temporal development of waves in the polar mlt region during stratospheric warmings. *Journal of Atmospheric and Solar-Terrestrial Physics*, *90*, 86–96. https://doi.org/10.1016/j.jastp.2012.04.004

Meinel, A. (1950). OH emission bands in the spectrum of the night sky. II. *The Astrophysical Journal*, *112*, 120, 112, 120. https://doi.org/10.1086/145321

Mertens, C. J., Mlynczak, M. G., López-Puertas, M., Wintersteiner, P. P., Picard, R., Winick, J. R., et al. (2001). Retrieval of mesospheric and lower thermospheric kinetic temperature from measurements of CO2 15 μm earth limb emission under non-LTE conditions. *Geophysical Research Letters*, *28*(7), 1391–1394. https://doi.org/10.1029/2000gl012189

Mitchell, N., Pancheva, D., Middleton, H., & Hagan, M. (2002). Mean winds and tides in the arctic mesosphere and lower thermosphere. *Journal of Geophysical Research*, *107*(A1). SIA-2. https://doi.org/10.1029/2001ja900127

Moffat-Griffin, T., Jarvis, M., Colwell, S., Kavanagh, A., Manney, G., & Daffer, W. (2013). Seasonal variations in lower stratospheric gravity wave energy above the Falkland Islands. *Journal of Geophysical Research: Atmospheres*, *118*(19), 10–861. https://doi.org/10.1002/jgrd.50859

Myrabø, H., Deehr, C., Viereck, R., & Henriksen, K. (1987). Polar mesopause gravity wave activity in the sodium and hydroxyl night airglow. *Journal of Geophysical Research*, *92*(A3), 2527–2534. https://doi.org/10.1029/ja092ia03p02527

Nakamura, T., Higashikawa, A., Tsuda, T., & Matsushita, Y. (1999). Seasonal variations of gravity wave structures in oh airglow with a CCD imager at Shigaraki. *Earth Planets and Space*, *51*(7–8), 897–906. https://doi.org/10.1186/bf03353248

Narayanan, V. L., Gurubaran, S., & Emperumal, K. (2009). Imaging observations of upper mesospheric nightglow emissions from Tirunelveli (8.7 ON). 92.60. HW; 92.60. HH; 92.60. HC. https://doi.org/10.1016/0021-9169(94)e0007-a

Nielsen, K., Taylor, M. J., Hibbins, R. E., Jarvis, M. J., & Russell, J. M. III. (2012). On the nature of short-period mesospheric gravity wave propagation over Halley, Antarctica. *Journal of Geophysical Research*, *117*(D5). https://doi.org/10.1029/2011JD016261

O'Sullivan, D., & Dunkerton, T. J. (1995). Generation of inertia–gravity waves in a simulated life cycle of baroclinic instability. *Journal of the Atmospheric Sciences*, *52*(21), 3695–3716. https://doi.org/10.1175/1520-0469(1995)052⟨3695:goiwia⟩2.0.co;2

Pallamraju, D., Baumgardner, J., Singh, R. P., Laskar, F. I., Mendillo, C., Cook, T., et al. (2014). Daytime wave characteristics in the mesosphere lower thermosphere region: Results from the balloon-borne investigations of regional-atmospheric dynamics experiment. *Journal of Geophysical Research: Space Physics*, *119*(3), 2229–2242. https://doi.org/10.1002/2013ja019368

Pautet, P. D., Taylor, M. J., Fritts, D. C., Janches, D., Kaifler, N., Dörnbrack, A., & Hormaechea, J. L. (2021). Mesospheric mountain wave activity in the lee of the southern Andes. *Journal of Geophysical Research: Atmospheres*, *126*(7), e2020JD033268. https://doi.org/10.1029/2020jd033268

Pautet, T., Michael, J., Eckermann, S. D., & Criddle, N. (2019). Regional distribution of mesospheric small-scale gravity waves during deepwave. *Journal of Geophysical Research: Atmospheres*, *124*(13), 7069–7081. https://doi.org/10.1029/2019jd030271

Pautet, T., Michael, J., Pendleton, W. R., Zhao, Y., Yuan, T., Esplin, R., & McLain, D. (2014). Advanced mesospheric temperature mapper for high-latitude airglow studies. *Applied Optics*, *53*(26), 5934–5943. https://doi.org/10.1364/ao.53.005934

Pautet, T., Michael, J., Snively, J. B., & Solorio, C. (2018). Unexpected occurrence of mesospheric frontal gravity wave events over south pole (90 s). *Journal of Geophysical Research: Atmospheres*, *123*(1), 160–173. https://doi.org/10.1002/2017jd027046

Pautet, & Moreels, G. (2002). Ground-based satellite-type images of the upper-atmosphere emissive layer. *Applied Optics*, *41*(5), 823–831. https://doi.org/10.1364/AO.41.000823

Perwitasari, S., Nakamura, T., Kogure, M., Tomikawa, Y., Ejiri, M. K., & Shiokawa, K. (2018). Comparison of gravity wave propagation directions observed by mesospheric airglow imaging at three different latitudes using the m-transform. In *Annales Geophysicae* (Vol. 36(6), pp. 1597–1605). https://doi.org/10.5194/angeo-36-1597-2018

Perwitasari, S., Nakamura, T., Tsugawa, T., Nishioka, M., Tomikawa, Y., Jin, H., et al. (2022). Propagation direction analyses of medium-scale traveling ionospheric disturbances observed over North America with GPS-TEC perturbation maps by three-dimensional spectral analysis method. *Journal of Geophysical Research: Space Physics*, *127*(1), e2020JA028791. https://doi.org/10.1029/2020ja028791

Pitteway, M., & Hines, C. (1974). The viscous damping of atmospheric gravity waves. *The Upper Atmosphere in Motion*, *18*, 363–391. https://doi.org/10.1029/gm018p0363

Pramitha, M., Ratnam, M. V., Taori, A., Murthy, B., Pallamraju, D., & Bhaskar Rao, S. V. (2015). Evidence for tropospheric wind shear excitation of high-phase-speed gravity waves reaching the mesosphere using the ray-tracing technique. *Atmospheric Chemistry and Physics*, *15*(5), 2709–2721. https://doi.org/10.5194/acp-15-2709-2015

Reichert, R., Kaifler, B., Kaifler, N., Rapp, M., Pautet, P.-D., Taylor, M. J., et al. (2019). Retrieval of intrinsic mesospheric gravity wave parameters using Lidar and airglow temperature and meteor radar wind data. *Atmospheric Measurement Techniques*, *12*(11), 5997–6015. https://doi.org/10.5194/amt-12-5997-2019

Reid, I. M., & Vincent, R. A. (1987). Measurements of the horizontal scales and phase velocities of short period mesospheric gravity waves at Adelaide, Australia. *Journal of Atmospheric and Terrestrial Physics*, *49*(10), 1033–1048. https://doi.org/10.1016/0021-9169(87)90110-3

Sato, K., Hashiguchi, H., & Fukao, S. (1995). Gravity waves and turbulence associated with cumulus convection observed with the uhf/vhf clear-air Doppler radars. *Journal of Geophysical Research*, *100*(D4), 7111–7119. https://doi.org/10.1029/95jd00198

Sato, K., Tateno, S., Watanabe, S., & Kawatani, Y. (2012). Gravity wave characteristics in the southern hemisphere revealed by a high-resolution middle-atmosphere general circulation model. *Journal of the Atmospheric Sciences*, *69*(4), 1378–1396. https://doi.org/10.1175/jas-d-11-0101.1

Scinocca, J., & Ford, R. (2000). The nonlinear forcing of large-scale internal gravity waves by stratified shear instability. *Journal of the Atmospheric Sciences*, *57*(5), 653–672. https://doi.org/10.1175/1520-0469(2000)057⟨0653:tnfols⟩2.0.co;2

Singh, R. P., & Pallamraju, D. (2016). Effect of cyclone Nilofar on mesospheric wave dynamics as inferred from optical nightglow observations from mount Abu, India. *Journal of Geophysical Research: Space Physics*, *121*(6), 5856–5867. https://doi.org/10.1002/2016ja022412

Singh, R. P., & Pallamraju, D. (2017). Near infrared imaging spectrograph (NIRIS) for ground-based mesospheric oh (6-2) and o 2 (0-1) intensity and temperature measurements. *Journal of Earth System Science*, *126*(6), 88. https://doi.org/10.1007/s12040-017-0865-4

Singh, R. P., Pallamraju, D., Suryawanshi, P., & Urmalia, S. (2023). Studies of atmospheric waves by ground-based observations of oh (3–1) emission and rotational temperature using PRL airglow infrared spectrograph (Pairs). *Journal of Atmospheric and Solar-Terrestrial Physics*, *244*, 106039. https://doi.org/10.1016/j.jastp.2023.106039

Suzuki, S., Shiokawa, K., Hosokawa, K., Nakamura, K., & Hocking, W. K. (2009). Statistical characteristics of polar cap mesospheric gravity waves observed by an all-sky airglow imager at resolute bay, Canada. *Journal of Geophysical Research*, *114*(A1). https://doi.org/10.1029/2008JA013652

Takahashi, H., Batista, P., Sahai, Y., & Clemesha, B. (1985). Atmospheric wave propagations in the mesopause region observed by the OH (8, 3) band, NaD, O2A (8645å) band and OI 5577 Å nightglow emissions. *Planetary and Space Science*, *33*(4), 381–384. https://doi.org/10.1016/0032-0633(85)90081-9

Takeo, D., Shiokawa, K., Fujinami, H., Otsuka, Y., Matsuda, T., Ejiri, M., et al. (2017). Sixteen year variation of horizontal phase velocity and propagation direction of mesospheric and thermospheric waves in airglow images at Shigaraki, Japan. *Journal of Geophysical Research: Space Physics*, *122*(8), 8770–8780. https://doi.org/10.1002/2017ja023919

Tashchilin, M., Beletsky, A., Mikhalev, A., Xu, J., & Yuan, W. (2010). Some results of observations of spatial inhomogeneities in the radiation of hydroxyl emissions. *Solar-Earth Physics*, *15*, 131–134. https://doi.org/10.1109/tap.1957.1144531

Taylor, M. J., Bishop, M. B., & Taylor, V. (1995). All-sky measurements of short period waves imaged in the oi (557.7 nm), NA (589.2 nm) and near infrared oh and O2 (0, 1) nightglow emissions during the aloha-93 campaign. *Geophysical Research Letters*, *22*(20), 2833–2836. https://doi.org/10.1029/95gl02946

Taylor, M. J., Pautet, P.-D., Fritts, D. C., Kaifler, B., Smith, S. M., Zhao, Y., et al. (2019). Large-amplitude mountain waves in the mesosphere observed on 21 June 2014 during deepwave: 1. Wave development, scales, momentum fluxes, and environmental sensitivity. *Journal of Geophysical Research: Atmospheres*, *124*(19), 10364–10384. https://doi.org/10.1029/2019jd030932

Taylor, M. J., Pendleton, W., Jr., Clark, S., Takahashi, H., Gobbi, D., & Goldberg, R. (1997). Image measurements of short-period gravity waves at equatorial latitudes. *Journal of Geophysical Research*, *102*(D22), 26283–26299. https://doi.org/10.1029/96jd03515

Taylor, M. J., Ryan, E., Tuan, T., & Edwards, R. (1993). Evidence of preferential directions for gravity wave propagation due to wind filtering in the middle atmosphere. *Journal of Geophysical Research*, *98*(A4), 6047–6057. https://doi.org/10.1029/92ja02604

Taylor, M. J., Turnbull, D., & Lowe, R. (1995). Spectrometric and imaging measurements of a spectacular gravity wave event observed during the aloha-93 campaign. *Geophysical Research Letters*, *22*(20), 2849–2852. https://doi.org/10.1029/95gl02948

Taylor, & Hapgood, M. (1988). Identification of a thunderstorm as a source of short period gravity waves in the upper atmospheric nightglow emissions. *Planetary and Space Science*, *36*(10), 975–985. https://doi.org/10.1016/0032-0633(88)90035-9

Taylor, & Hill, M. (1991). Near infrared imaging of hydroxyl wave structure over an ocean site at low latitudes. *Geophysical Research Letters*, *18*(7), 1333–1336. https://doi.org/10.1029/91gl01299

Taylor, & Pautet (2024). OH (3-1) band intensity maps from advanced mesospheric temperature mapper (AMTM) January 2014 - January 2016 (Norway) (Version 1.0) [Dataset]. *NERC EDS UK Polar Data Centre*. https://doi.org/10.5285/c69e740e-470e-4afa-9ae1-05d54c4aa80d

Thompson, D., & Wallace, J. (1998). The arctic oscillation signature in wintertime geopotential height and temperature fields. *Geophysical Research Letters*, *25*(9), 1297–1300. https://doi.org/10.1029/98gl00950

Thurairajah, B., Collins, R. L., Harvey, V. L., Lieberman, R. S., & Mizutani, K. (2010). Rayleigh Lidar observations of reduced gravity wave activity during the formation of an elevated stratopause in 2004 at Chatanika, Alaska (65 n, 147 w). *Journal of Geophysical Research*, *115*(13). https://doi.org/10.1029/2009jd013036

Tomikawa, Y. (2015). Gravity wave transmission diagram. In *Annales Geophysicae* (Vol. 33(12), pp. 1479–1484). https://doi.org/10.5194/angeo-33-1479-2015

Tsuchiya, S., Shiokawa, K., Fujinami, H., Otsuka, Y., Nakamura, T., Connors, M., et al. (2019). Three-dimensional fourier analysis of the phase velocity distributions of mesospheric and ionospheric waves based on airglow images collected over 10 years: Comparison of Magadan, Russia, and Athabasca, Canada. *Journal of Geophysical Research: Space Physics*, *124*(10), 8110–8124. https://doi.org/10.1029/2019ja026783

Tsuchiya, S., Shiokawa, K., Fujinami, H., Otsuka, Y., Nakamura, T., & Yamamoto, M. (2018). Statistical analysis of the phase velocity distribution of mesospheric and ionospheric waves observed in airglow images over a 16-year period: Comparison between Rikubetsu and Shigaraki, Japan. *Journal of Geophysical Research: Space Physics*, *123*(8), 6930–6947. https://doi.org/10.1029/2018ja025585

Vadas, S. L. (2007). Horizontal and vertical propagation and dissipation of gravity waves in the thermosphere from lower atmospheric and thermospheric sources. *Journal of Geophysical Research*, *112*(A6). https://doi.org/10.1029/2006ja011845

Vadas, S. L., Becker, E., Bossert, K., Baumgarten, G., Hoffmann, L., & Harvey, V. L. (2023). Secondary gravity waves from the stratospheric polar vortex over Alomar observatory on 12–14 January 2016: Observations and modeling. *Journal of Geophysical Research: Atmospheres*, *128*(2), e2022JD036985. https://doi.org/10.1029/2022jd036985

Vadas, S. L., & Fritts, D. C. (2005). Thermospheric responses to gravity waves: Influences of increasing viscosity and thermal diffusivity. *Journal of Geophysical Research*, *110*(D15). https://doi.org/10.1029/2004jd005574

Vincent, R. (1984). Gravity-wave motions in the mesosphere. *Journal of Atmospheric and Terrestrial Physics*, *46*(2), 119–128. https://doi.org/10.1016/0021-9169(84)90137-5

von Savigny, C., McDade, I., Eichmann, K.-U., & Burrows, J. (2012). On the dependence of the OH* Meinel emission altitude on vibrational level: SCIAMACHY observations and model simulations. *Atmospheric Chemistry and Physics*, *12*(18), 8813–8828. https://doi.org/10.5194/acp-12-8813-2012

Wallace, L. (1962). The OH nightglow emission. *Journal of the Atmospheric Sciences*, *19*(1), 1–16. https://doi.org/10.1175/1520-0469(1962)019⟨0001:tone⟩2.0.co;2

Wrasse, C. M., Nyassor, P. K., da Silva, L. A., Figueiredo, C. A., Bageston, J. V., Naccarato, K. P., et al. (2024). Studies on the propagation dynamics and source mechanism of quasi-monochromatic gravity waves observed over São Martinho da Serra (29 S, 53 W), Brazil. *Atmospheric Chemistry and Physics*, *24*(9), 5405–5431. https://doi.org/10.5194/acp-24-5405-2024

Wright, C. J., Hindley, N. P., Hoffmann, L., Alexander, M. J., & Mitchell, N. J. (2017). Exploring gravity wave characteristics in 3-D using a novel s-transform technique: Airs/aqua measurements over the southern Andes and Drake Passage. *Atmospheric Chemistry and Physics*, *17*(13), 8553–8575. https://doi.org/10.5194/acp-17-8553-2017

Wüst, S., Bittner, M., Espy, P. J., French, W. J. R., & Mulligan, F. J. (2023). Hydroxyl airglow observations for investigating atmospheric dynamics: Results and challenges. *Atmospheric Chemistry and Physics*, *23*(2), 1599–1618. https://doi.org/10.5194/acp-23-1599-2023

Wüst, S., Schmidt, C., Hannawald, P., Bittner, M., Mlynczak, M. G., & Russell, J. M. III. (2019). Observations of oh airglow from ground, aircraft, and satellite: Investigation of wave-like structures before a minor stratospheric warming. *Atmospheric Chemistry and Physics*, *19*(9), 6401–6418. https://doi.org/10.5194/acp-19-6401-2019

Yiğit, E., Medvedev, A. S., Aylward, A. D., Hartogh, P., & Harris, M. J. (2009). Modeling the effects of gravity wave momentum deposition on the general circulation above the turbopause. *Journal of Geophysical Research*, *114*(D7). https://doi.org/10.1029/2008jd011132

Yoshiki, M., Kizu, N., & Sato, K. (2004). Energy enhancements of gravity waves in the Antarctic lower stratosphere associated with variations in the polar vortex and tropospheric disturbances. *Journal of Geophysical Research*, *109*(D23). https://doi.org/10.1029/2004jd004870

Yoshiki, M., & Sato, K. (2000). A statistical study of gravity waves in the polar regions based on operational radiosonde data. *Journal of Geophysical Research*, *105*(D14), 17995–18011. https://doi.org/10.1029/2000jd900204

Yuan, T., Pautet, P.-D., Zia, K., Zhao, Y., & Taylor, M. (2024). The variations of gravity wave activities during the formation of the large horizontal wind shears in the static state lower thermosphere. *Earth and Space Science*, *11*(4), e2023EA003296. https://doi.org/10.1029/2023ea003296

Zhao, Y., Taylor, M. J., Pautet, P.-D., Moffat-Griffin, T., Hervig, M. E., Murphy, D. J., et al. (2019). Investigating an unusually large 28-day oscillation in mesospheric temperature over Antarctica using ground-based and satellite measurements. *Journal of Geophysical Research: Atmospheres*, *124*(15), 8576–8593. https://doi.org/10.1029/2019jd030286